

THE MASS AND ABSORPTION COLUMNS OF GALACTIC GASEOUS HALOS

ZHIJIE QU AND JOEL N. BREGMAN

Department of Astronomy, University of Michigan, Ann Arbor, MI 48104, USA

Draft version February 16, 2018

ABSTRACT

The galactic gaseous halo is a gas reservoir for the interstellar medium in the galaxy disk, supplying materials for star formation. We developed a gaseous halo model connecting the galaxy disk and the gaseous halo by assuming that the star formation rate on the disk is balanced by the radiative cooling rate of the gaseous halo, including stellar feedback. In addition to a single-temperature gaseous halo in collisional ionization equilibrium, we also consider the photoionization effect and a steady-state cooling model. Photoionization is important for modifying the ion distribution in low-mass galaxies and outskirts of massive galaxies due to the low densities. The multi-phase cooling model dominates the region within the cooling radius, where $t_{\text{cooling}} = t_{\text{Hubble}}$. Our model reproduces most of the observed high ionization state ions for a wide range of galaxy masses (i.e., O VI, O VII, Ne VIII, Mg X, and O VIII). We find that the O VI column density has a narrow range around $\approx 10^{14} \text{ cm}^{-2}$ for halo masses from $M_{\star} \approx 3 \times 10^{10} M_{\odot}$ to $6 \times 10^{12} M_{\odot}$, which is consistent with some but not all observational studies. For galaxies with halo masses $\lesssim 3 \times 10^{11} M_{\odot}$, photoionization produces most of the O VI, while for more massive galaxies, the O VI is from the medium that is cooling from higher temperatures. Fitting the Galactic (Milky-Way) O VII and O VIII suggests a gaseous halo model where the metallicity is $\approx 0.55 Z_{\odot}$ and the gaseous halo has a maximum temperature of $\approx 1.9 \times 10^6 \text{ K}$. This gaseous halo model does not close the census of baryonic material within R_{200} .

Subject headings: galaxies: halos – galaxies: CGM – galaxies: X-ray – quasars: absorption lines

1. INTRODUCTION

Recently, more and more observational evidence has been found to show the importance of gaseous components (the circumgalactic medium; CGM) in galaxy halos (Anderson & Bregman 2010; Ménard et al. 2010; Werk et al. 2014; see the review of Tumlinson et al. 2017). These gaseous components surrounding the galaxy disk are formed during the galaxy formation and are modified by various feedback processes, such as stellar feedback and active galactic nucleus (AGN) feedback (White & Frenk 1991). The existence of a CGM also modifies the evolution of the galaxy by providing fresh materials for star formation (Kereš et al. 2005; Sancisi et al. 2008; Kereš et al. 2009), and by heating materials accreted from the intergalactic medium (IGM) through the gravitational potential release and the accretion shock (Mo et al. 2010).

The existence of gaseous halos is also helpful to explain various observational issues, such as the missing baryon problem (the baryonic fraction is significantly lower than the cosmic baryonic fraction of 0.16; Dai et al. 2010; McGaugh & Schombert 2015; Planck Collaboration et al. 2016). One solution is that the missing baryons stay in the galaxy but in an invisible phase (low density and high temperature), which could be the hot gaseous halo (Fukugita & Peebles 2006; Bregman & Lloyd-Davies 2007). Theoretically, simulations found that the cool gas (10^4 K) in the early Universe ($z > 4$) is heated, becoming a warm-hot intergalactic medium ($10^5 - 10^7 \text{ K}$) during galaxy formation, which accounts for more than 30% of total baryons (Weinberg et al. 1997; Cen & Ostriker

1999).

The final temperature of these heating processes is about the virial temperature of the galaxy, which is determined by the galaxy halo mass. Massive galaxies have higher virial temperatures than low-mass galaxies, and the virial temperature of low-mass galaxies ($M_{\text{h}} \sim 10^{11} M_{\odot}$) is around $10^{5.5} \text{ K}$, which is also the peak temperature of the radiative cooling curve and can lead to rapid cooling with a cooling timescale of $< 1 \text{ Gyr}$. Therefore, whether the gaseous halo exists is a result of the competition between various heating processes and the radiative cooling, and this competition results in a multi-phase medium in the gaseous halo (Oppenheimer et al. 2016).

Multi-wavelength observations of both emission and absorption reveal different phase mediums in the gaseous halo. The hot components in the gaseous halo can be detected in emission by direct X-ray imaging (Anderson & Bregman 2010; Bogdán et al. 2013; Goulding et al. 2016; Li et al. 2016), and in absorption or emission from high ionization state ions (e.g., O VII, Ne VIII and Mg X; Nicastro et al. 2002; Savage et al. 2005; Miller & Bregman 2015; Qu & Bregman 2016). These studies found that the mass of the hot gaseous halo is comparable to the stellar mass of the galaxy, and about half of total baryons are still missing. Some studies show that the hot gas may account for all missing baryons in the Milky Way (MW; Gupta et al. 2012; Nicastro et al. 2016a), however, they overestimate the emission measurement by more than one order of magnitude (Bregman et al. 2018; Li & Bregman 2018). Ultraviolet (UV) absorption line studies on low and intermediate ionization state ions show the existence of cool clouds in the halos, but the mass is model-dependent with a variation from 6% to

40% of the total baryon mass (Werk et al. 2014; Stern et al. 2016).

With a large amount of gas in the halo, radiative cooling may lead to a significant cooling flow onto the galaxy disk, which will be transformed into the stellar content of the disk through star formation (Sancisi et al. 2008). This astrophysical connection between the radiative cooling and the star formation suggests that the cooling rate and the star formation rate (SFR) should be comparable with each other. Although the net cooling rate is also modified by heating from galactic feedback or accretion from the IGM, observations showed that the cooling rate is approximately the SFR for star-forming galaxies (with large scatter; Li et al. 2014).

In this paper, our starting point is that the SFR is balanced by the radiative cooling rate of the gaseous halo within the cooling radius. Then, we employ a set of assumptions for the gaseous halo – the density profile, the temperature distribution, hydrostatic and ionization equilibrium, and build up a halo model to connect the properties of the gaseous halo (i.e., mass and ion column density) to other galaxy properties (i.e., stellar mass and star formation rate). The details of the model assumptions are described in Section 2. In Section 3, we present the mass and column density of the gaseous halos, and their dependence on model parameters (e.g., stellar mass, SFR, or metallicity). The comparison with observations and implications are discussed in Section 4; our results are summarized in Section 5.

2. MODEL

We consider a spherical volume-filling gaseous halo model to connect the galaxy properties with the gaseous halo properties. In this section, the employed assumptions will be described and discussed.

2.1. General Picture

During the formation of the galaxy, the accreted material is heated by the released gravitational potential through the accretion shock. Without radiative energy losses, the final temperature of a gravitationally self-bound system is the virial temperature that is determined by the total mass. However, a realistic gaseous halo suffers from radiative cooling, which is crucial for the formation of galaxy disk.

Once the galaxy disk is formed, star formation leads to stellar feedback, injecting gas, dust, and energy into the gaseous halo. Stellar feedback affects the galaxy in several ways: stellar winds of massive stars; mass-loss of asymptotic giant branch stars; and supernovae from either massive stars or degenerate stars (Zaritsky et al. 1994; Willson 2000; Scannapieco et al. 2008). Another main feedback channel is the central supermassive black hole that is in an active galactic nuclei (AGN) phase, which injects ionizing photons and high-energy particles (Fabian 2012). These feedback processes can offset radiative cooling, or reheat the cooled gas (Li et al. 2015). Although these processes are poorly resolved and implemented with different subgrid models in cosmological simulations, their effects on the galaxy evolution have been confirmed showing that no single feedback channel can dominate across all galaxy masses (Vogelsberger et al. 2014; Schaye et al. 2015; Hopkins et al. 2017). However, the relative contributions for different processes are

still controversial (Nelson et al. 2017; Suresh et al. 2017).

Besides the feedback from the galaxy disk, accretion from the IGM also provides additional energy to the gaseous halo as material falls deeper into the gravitational potential well. Then, the energy conservation of the gaseous halo leads to

$$L_{\text{net,cl}} = L_{\text{rad}} - L_{\text{net,acc}} - L_{\text{fb}}, \quad (1)$$

where symbols denote the net cooling, the radiative cooling, the net accretion heating and the feedback heating. For simplicity, we ignore the heating from the accretion of the IGM gas in our models, since the actual value of accretion heating depends on several uncertain factors – the accretion rate from IGM, the accretion shock process and the structure around the virial radius. However, an estimation shows that the contribution from accretion heating is not significant when the hot gaseous halo already exists. Assuming the accreted material is virialized at the virial radius, the released gravitational potential energy is $2k_{\text{B}}T_{\text{vir}}$, which is slightly larger than the internal energy of the virialized halo of $3/2k_{\text{B}}T_{\text{vir}}$. Additionally, the energy to ionize electrons from atoms will increase the internal energy by several tens of eV per atom, which is equivalent to a temperature around $10^5 - 10^6$ K (depending on the ionization state that is proportional to the virial temperature). Therefore, the energy used to ionize atoms cannot be transformed into internal energy, which decreases the net heating from the IGM accretion. Finally, we consider the net cooling rate that is only related to the radiative cooling and the heating due to galactic feedback.

The net cooling flux is related to the accretion flow since the cooled gas cannot be buoyant in the halo due to the gravitational potential. Once the gas from the halo is accreted onto the disk, it will interact with the disk interstellar medium or outflows launched from the disk, which leads to the disruption of the cool gas and the condensation of the hot gas (Marinacci et al. 2010; Scannapieco & Brüggén 2015). Additionally, various processes are involved in this interaction, such as the disk dynamics and the thermal conduction, which lead to complex situations in different galaxies (Oosterloo et al. 2007; Armillotta et al. 2016; Zheng et al. 2017). These phenomenon are beyond the scope of this paper, therefore, we assume that the accreted cold gas could be mixed with the existed ISM instantly to avoid detailed interactions between disk and halo gases.

Studies of the MW molecular clouds showed that the star formation timescale is comparable to the dynamical timescale of the cloud ($\sim 1 - 10$ Myr), and the star formation efficiency is less than 2% (Larson 1981; Myers et al. 1986; Leroy et al. 2008). Considering the SFR of the MW as $\approx 1 M_{\odot} \text{ yr}^{-1}$ (Robitaille & Whitney 2010), around $100 M_{\odot} \text{ yr}^{-1}$ gas should be transformed into the star-forming molecular clouds since the lifetime of molecular clouds is short ($\lesssim 20$ Myr; Larson 1981, 1994). The total atomic gas mass in the MW is around $7 \times 10^9 M_{\odot}$ (Nakanishi & Sofue 2016), which means that the atomic gas will be refreshed in around 70 Myr. Therefore, the timescale is around several 10^7 yr to form stars using accreted cool gas from the gaseous halo. This timescale is comparable with the timescale of current measurement methods (i.e., UV/IR) of SFR for external galaxies, which measure the

average SFR over 10^7 to 10^8 yr (Madau & Dickinson 2014). In this sense, the measured net cooling flow mass has a physical connection with the measured SFR.

The cold mode accretion provides an additional gas origin besides the hot mode accretion (the radiative cooling and accretion of the virialized halo), which requires the density of at least one order of magnitude higher than n_{200} ($10^{-3} - 10^{-4} \text{ cm}^{-3}$) and the low temperature (10^{4-5} K) for the gas to remain cool during the accretion (Kereš et al. 2005). The cold mode accretion leads to cool gas filaments in the halo, directly connecting the disk and the IGM and transporting gases into the disk (Kereš et al. 2009). However, the existence of a hot ambient halo ($T \approx T_{\text{vir}}$) near hydrostatic equilibrium could destroy these cold gas filaments by the mixing and interaction, which makes the contribution from the cold mode accretion less than one-third of the hot mode in the low redshift universe ($z < 2$; Nelson et al. 2013). Therefore, involving cold mode accretion will not break the balance between the cooling flow and the star formation, so we adopt the assumption that the net cooling rate is equal to the SFR.

Feedback processes must be included, as they will offset some of the radiative cooling. For a star-forming galaxy without a merger, the gas for star formation is originally from the gaseous halo, and the accretion from a gaseous halo is modified by the strength of stellar feedback (i.e., proportional to the SFR) when the redshift is low. Therefore, for a galaxy dominated by stellar feedback (with a dim AGN or without an AGN), the stellar feedback strength is proportional to the radiative cooling rate, which can be modeled as $\dot{M}_{\text{stellar,h}} = \alpha \dot{M}_{\text{rad,cl}}$. Then, a simple relationship between the SFR and the radiative cooling rate is

$$\text{SFR} = \gamma \dot{M}_{\text{rad,cl}}, \quad (2)$$

where $\gamma = 1 - \alpha$ is smaller than unity to account the heating by stellar feedback, and $\dot{M}_{\text{rad,cl}}$ is the total radiative cooling rate of the gaseous halo. For simplicity, we assume that γ is unity for the following calculation; the effect of variations in this γ factor is discussed in Section 4.

This relationship will be broken by several physical processes, such as feedback from an AGN or a starburst event. For AGN feedback, there is no direct connection with the SFR, therefore, there is no direct relationship between AGN feedback heating and the radiative cooling. For merging galaxies that trigger starburst events, the connection between the SFR and the radiative cooling rate is not valid either, since the interaction between gases in the two galaxies triggers the star formation, which is not related to the gaseous halo cooling. Therefore, Equation (2) is only applicable for stably-evolving star-forming galaxies without powerful AGNs.

Therefore, in our model, the SFR and radiative cooling from the gaseous halo are tightly connected. This model is most applicable to field galaxies, rather than group or cluster galaxies, which can be greatly affected by the intragroup or intracluster medium (Balogh et al. 1998). With these constraints, we adopt the conditions where the SFR is equal to the radiative cooling rate of the gaseous halo. The radiative cooling rate is limited within the cooling radius, where the cooling timescale is equal to

the Universe age (13.8 Gyr; Planck Collaboration et al. 2016) or the cosmic epoch at a given redshift. In the following calculation, we use $H_0 = 67.8 \text{ km s}^{-1} \text{ Mpc}^{-1}$, $\Omega_{\text{m}} = 0.308$, and $\Omega_{\text{b}} = 0.0483$ (Planck Collaboration et al. 2016).

2.2. Galaxy and Gaseous Halo Properties

To construct sample galaxies, we adopt several empirical relationships. For a given stellar mass, we obtain the halo mass based on the stellar mass-halo mass (SMHM) relationship (Behroozi et al. 2013; Kravtsov et al. 2014). These two SMHM relationships diverge when $M_{\text{h}} > 10^{11.5} M_{\odot}$, and Kravtsov et al. (2014) has a higher stellar mass than Behroozi's relationship. At the halo mass of $10^{13.5} M_{\odot}$, the stellar mass difference is around 0.5 dex. We choose the Kravtsov's SMHM relationship, since it describes the case that is more similar to the MW, where a $\approx 2 \times 10^{12} M_{\odot}$ halo hosts a $5 - 8 \times 10^{10} M_{\odot}$ galaxy disk. Once the halo mass is determined, the virial radius and the virial temperature are calculated as:

$$\begin{aligned} R_{\text{vir}} = R_{200} &= \frac{M_{\text{h}}}{4\pi\Delta_{\text{vir}}\rho_{\text{crit}}/3}, \\ V_{\text{c}}^2 &= \frac{GM_{\text{h}}}{R_{\text{vir}}} = 100H_0^2 R_{\text{vir}}^2, \\ T_{\text{vir}} &= \frac{\mu m_{\text{p}} V_{\text{c}}^2}{2k_{\text{B}}}, \end{aligned} \quad (3)$$

where $\Delta_{\text{vir}} = 200$ is the collapse factor, and $\rho_{\text{crit}} = 3H_0^2/8\pi G$ is the cosmic critical density. The quantities R_{vir} and T_{vir} are input parameters of our models and can be varied by introducing additional factors (as the model of the MW in Section 4.5). Therefore, the choice of the SMHM relationship does not affect our results significantly.

The star formation rate can be inferred using the star formation-stellar mass plane (Renzini & Peng 2015; Morselli et al. 2016):

$$\log(\text{SFR}) = (0.72 \pm 0.02) \log M_{\star} - 7.12, \quad (4)$$

in the stellar mass range of $M_{\star} = 10^{8.5} - 10^{11.25} M_{\odot}$. Therefore, we set the range of halo mass to $10^{10.5} - 10^{13.5} M_{\odot}$. The star formation also has a dependence on the redshift (Pannella et al. 2009):

$$\overline{\text{SFR}} \approx 270 \frac{M_{\star}}{10^{11} M_{\odot}} \left(\frac{t}{3.4 \times 10^9 \text{ yr}} \right)^{-2.5} \frac{M_{\odot}}{\text{yr}}, \quad (5)$$

where t is the cosmic epoch. This relationship can be rewritten as a dependence on the redshift directly $\text{sSFR} \propto (1+z)^3$ at $z < 2$ (Lilly et al. 2013).

The structure of the gaseous halo is also fixed to reduce the degree of freedom, and we adopt the β -model for gaseous halos for all galaxies with different masses, which has the density profile:

$$\rho(r) = n_0 \left(1 + \frac{r^2}{r_c^2} \right)^{-3\beta/2}, \quad (6)$$

where n_0 is the normalization parameter, and r_c is the core radius. Normally, core radii for galaxies are small, and cannot be modeled for isolated galaxies (Li et al.

2016). Then, we rewrite the profile as

$$\rho(r) = \frac{n_0 r_c^{3\beta}}{r^{3\beta}}, \quad (7)$$

which is valid for $r \gg r_c$, and then the degeneracy of $n_0 r_c^{3\beta}$ will not be broken. X-ray imaging studies on nearby massive galaxies showed that the β factor is around 0.5 within the radius ≤ 50 kpc (Anderson et al. 2016). Recently, the Circum-Galactic Medium of Massive Spirals (CGM-MASS) project shows that β is a constant of ≈ 0.4 extended to around the half of virial radius (≈ 200 kpc for massive star-forming spiral galaxies; Li et al. 2017). Therefore, we adopted β as a constant over all of the radius range for one gaseous halo, but β can be varied for different models.

Since the total mass of the β -model is not convergent with increasing radius, we need to set the radius range for this model. In the inner region, other physical processes occur (e.g., the interaction with disk gases), therefore, the hydrostatic assumption is broken, and the β -model may not be applicable. This radius is set by the competition between the free-fall timescale and the radiative cooling timescale, which is around 5 – 10 kpc using the radiative cooling timescale of the MW from Miller & Bregman (2015). Massive galaxies have larger inner radii that can be larger than 10 kpc, but our model does not show significant dependence on the innermost radius. From 5 kpc to 10 kpc, the mass of the gaseous halo is increased by up to 15%, which is only for the most massive galaxies ($M_h > 10^{13} M_\odot$) due to their small cooling radii. For L^* galaxies, this change is smaller than 10%, therefore, we fix the innermost radius as 5 kpc for all galaxies. For the outer region, the maximum radius is set to the virial radius for a given halo mass, which means that the density goes to zero at the virial radius. However, it is shown that the massive system (galaxy cluster) could have detectable gas reaching R_{200} , which implies that the gaseous component could extend beyond the virial radius (Baldi et al. 2012). Therefore, this assumption may not be correct, however, there are no other means to set an unbiased boundary condition.

The normalization parameter n_0 is calculated based on the assumption that the SFR is equal to the radiative cooling rate:

$$\text{SFR} = \int_{5\text{kpc}}^{\min\{R_{200}, R_{\text{cl}}\}} \frac{\bar{\Lambda}(r)n^2(r)}{\bar{\epsilon}(r)} \mu m_p 4\pi r^2 dr, \quad (8)$$

where $\bar{\Lambda}(r)$ is the average radiative cooling emissivity, while the $\bar{\epsilon}(r)$ is the average internal energy at a given radius, defining as

$$\bar{\Lambda} = \frac{\int_{T_{\min}}^{T_{\max}} M(T)n(T)\Lambda(T)dT}{\int_{T_{\min}}^{T_{\max}} M(T)n(T)dT}, \quad (9)$$

$$\bar{\epsilon} = \int_{T_{\min}}^{T_{\max}} M(T) \frac{3}{2} k_B T dT. \quad (10)$$

$M(T)$ is the mass distribution depending on the temperature, which has the normalization of $\int_{T_{\min}}^{T_{\max}} M(T)dT = 1$. Here, we also assume that the average mass of particles (μ) is 0.59 for the temperature range considered

($T > 10^{4.5}$ K), since this value is dominated by the ionization state of the hydrogen, which is almost completely ionized in this temperature range. The choice on the radiative cooling model will be discussed in the following section.

The radial dependence of temperature is still observationally poorly constrained for isolated galaxies. X-ray studies on galaxy clusters showed that the temperature variation is less than one order of magnitude within R_{500} (Baldi et al. 2012). For isolated star-forming galaxies, Anderson et al. (2016) showed that NGC 1961 also has a small variation, but only out to ~ 50 kpc. Here, we assume that there is no radius-dependence of the temperature.

2.3. Cooling Emissivity

The radiative cooling rate is directly affected by the emissivity, which has a dependence on the temperature, the density and the metallicity. For the temperature range of a gaseous halo ($\sim 10^{4.5} - 10^7$ K), the radiative cooling is dominated by lines of various ions. Therefore, for a given temperature and density, the ionization state of different ions can be determined and the cooling rate is calculated involving the metallicity. Here, we assume that the gaseous halo is in ionization equilibrium, and consider two ionization processes – collisional ionization and the modification due to photoionization.

For collisional ionization equilibrium (CIE), we adopt the emissivity calculated using CHIANTI (version 8.0.6; Del Zanna et al. 2015). In this calculation, the metallicity is set to 0.1 Z_\odot , 0.3 Z_\odot , 1.0 Z_\odot and 2.0 Z_\odot , and the solar metallicity of $Z_\odot = 0.0142$ is adopted from Asplund et al. (2009).

The photoionization due to the ultraviolet background (UVB) can modify the ionization distribution of different elements (Wiersma et al. 2009), and the photoionization model is employed to model the low and intermediate ionization ions in intervening systems (Savage et al. 2014; Werk et al. 2014). Also, the high ionization state ions might be photoionized at low densities of $\lesssim 10^{-5} \text{ cm}^{-3}$, which is the expected density in the outskirts of gaseous halos (Hussain et al. 2015, 2017). Therefore, we include the photoionization from the UVB to compare with the pure collisional ionization mode.

Galaxies also provide a part of the ionizing flux to photoionize the CGM or nearby IGM, which is known as the escaping ionizing flux. The escape fraction is believed to be large ($\gtrsim 10\%$) in the early Universe ($z > 6$) to contribute to the re-ionization (Mitra et al. 2013), while studies of the low redshift IGM ($z < 2$) found the escape fraction is several percent (Khaire & Srianand 2015). The small escape fraction has the implication that those ionizing photons mainly affect the innermost ~ 50 kpc region of the gaseous halo, thus, we ignore ionizing photons from the galaxy disk (Suresh et al. 2017).

For the photoionization equilibrium (PIE), we adopt the calculation from Oppenheimer & Schaye (2013), who tabulated results for different redshifts, densities, and temperatures. Several UVB models have been provided, and we choose the UVB form Haardt & Madau (2012) in our models. In this database, authors also include the cosmic microwave background (CMB), with the dependence on the redshift. The existence of the CMB provides a large number of low-energy photons, which

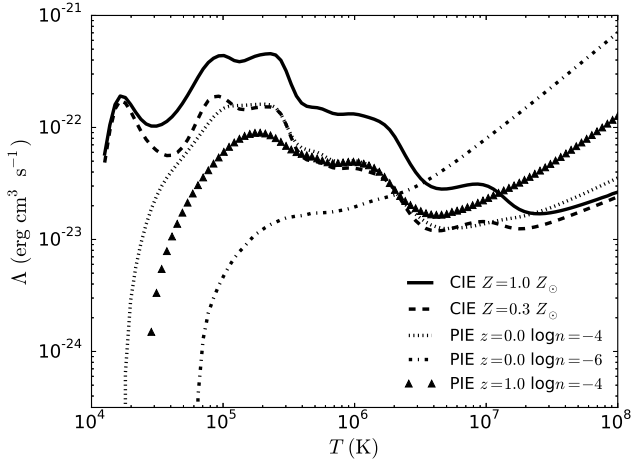


FIG. 1.— Comparison between the cooling curve for pure collisional ionization (CIE) and with the modification from photoionization (PIE). The cooling curves in CIE have metallicities of $1 Z_{\odot}$ (the solid line) and $0.3 Z_{\odot}$ (the dashed line). The three PIE cooling curves all have the same metallicity of $0.3 Z_{\odot}$. The dotted line has a density of 10^{-4} cm^{-3} (typical of the density of the inner gaseous halo) and at $z = 0$, while the dash-dotted line has a lower density of 10^{-6} cm^{-3} (typical of the density in the halo outskirts) at the same redshift. The up-triangle shows the cooling curve at $z = 1$ with a density of 10^{-4} cm^{-3} .

can be heated by inverse Compton scattering, thereby cooling the high-temperature electrons.

In Fig. 1, we show the comparison between CIE and PIE cooling curves. High energy photons from the UVB photoionize low ionization state ions to higher states, which suppresses the cooling in the low-temperature region. Due to the lack of H I, the first peak around $2 \times 10^4 \text{ K}$ is missing. The photoionization also changes the ionization fraction of metals and contributions to the radiative cooling, suppressing low ionization state cooling (e.g., C II and O II) and increasing high ionization cooling (e.g., O VI). Therefore, the cooling emissivity is lower in the low-temperature regime for the PIE model than the CIE model. Inverse Compton cooling due to CMB dominates the high temperature and low-density gas. The emissivity of inverse Compton scattering is proportional to nT , while the free-free emission has the dependence $n^2 T^{1/2}$. Therefore, there is always a critical combination of temperatures and densities, above which the inverse Compton cooling is dominant. However, in the low redshift Universe ($z < 2$), the number density of CMB photons is sufficiently low so that gases have a cooling timescale longer than the Hubble timescale. Therefore, the effect due to the CMB can be ignored for the low redshift ($z < 2$) Universe. The effect of the radiative cooling model will be described in details in Section 3.

2.4. Temperature Dependence of the Mass Distribution

Multi-phase gas in gaseous halos have been detected by various observations (Nicastro et al. 2002; Danforth & Shull 2008; Anderson et al. 2013; Werk et al. 2013; Savage et al. 2014; Qu & Bregman 2016). Unfortunately, obtaining an accurate distribution of the multi-phase medium by mass remains a challenge both observationally or theoretically (e.g., the divergence on O VI abundance; Oppenheimer et al. 2016; Suresh et al. 2017). Therefore, for

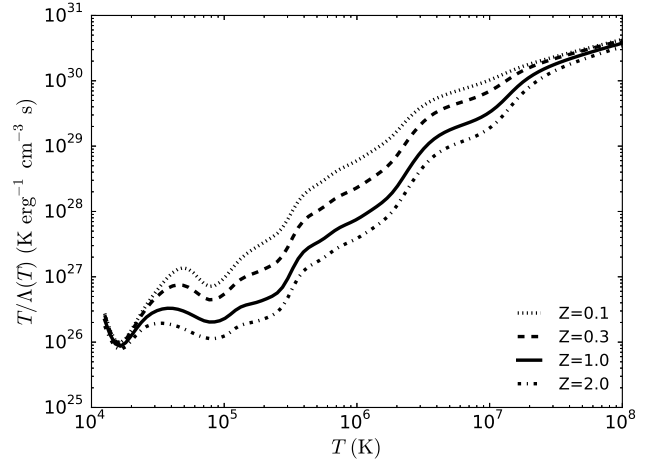


FIG. 2.— The unnormalized mass distribution for cooling gas as a function of temperature. CIE cooling curves with metallicities of $0.1 Z_{\odot}$, $0.3 Z_{\odot}$, $1.0 Z_{\odot}$ and $2.0 Z_{\odot}$ are shown in dotted, dashed, solid and dot-dashed lines, respectively. With temperature limits, which are related to the galaxy mass, this function can be normalized as $\int_{T_{\min}}^{T_{\max}} M(T) dT = 1$ to obtain the mass distribution $M(T)$.

the simplest model, we assume that the gaseous halo is a single phase medium at the virial temperature.

We also consider a stable cooling model, which is a time-independent solution. In this model, we assume the mass cooling rate is the same at all temperatures:

$$L(T) = \Lambda(T) n^2(T) \frac{M(T)}{\mu m_p n(T)} = \text{const.}, \quad (11)$$

where $L(T)$ is the luminosity at a given temperature T , and $M(T)$ is the mass distribution dependence on the temperature. Another assumption is the pressure balance, which implies $n(T) \propto 1/T$. Thus, the mass distribution is

$$M(T) = \frac{T}{\Lambda(T)} / \int_{T_{\min}}^{T_{\max}} \frac{T}{\Lambda(T)} dT, \quad (12)$$

the temperature upper limit (T_{\max}) is set to the virial temperature, while the lower limit is fixed to $10^{4.5} \text{ K}$, under which forbidden lines dominate the cooling, along with dust and molecules. An example of $M(T)$ without normalization is shown in Fig. 2.

Our model does not include all relevant physics that occurs in galaxy halos (e.g., thermal instabilities), but it allows us to explore a wide range of parameter space and to identify robust results. Detailed calculations show that the stable cooling model has applicability for the cooling in a temperature range of 10^4 K to $10^{6.5} \text{ K}$ in stellar feedback dominated galaxies (Thompson et al. 2016). Their breaking of this cooling assumption in the high-temperature range is mainly because they consider the hot gas from the stellar feedback, which softens the assumed boundary condition that the high-temperature gas can be supplied infinitely. However, in the gaseous halo scenario, this condition could be satisfied when a hot and long radiative-cooling timescale gaseous halo exists.

3. RESULTS

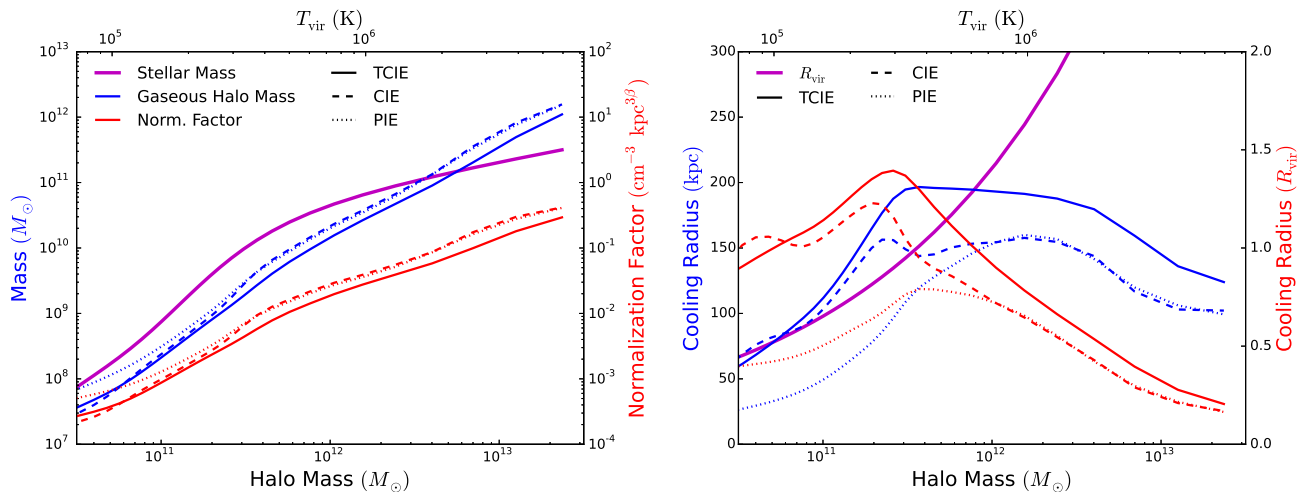


FIG. 3.— *Left panel:* The gaseous halo mass and the normalization factor of different models at $z = 0$. The blue lines are the gaseous halo masses, while the red lines are the normalization factors in the β -model. CIE, PIE and TCIE models are shown in dash-dotted, dashed, and solid lines. The magenta line is the stellar mass from stellar mass-halo mass relationship (Kravtsov et al. 2014). *Right panel:* The cooling radius, the radius within which the cooling time equals the local Hubble time, as a function of halo mass. The blue lines are the absolute cooling radius (left scale), while the red lines are the cooling radius in the unit of the virial radius (right scale). The range in the cooling radius only changes by a factor of four over the range in which the halo mass changes by three orders of magnitude.

We calculate three models with different cooling models and temperature distributions – CIE: the single temperature collisional ionization model; PIE: the single temperature photoionization model; TCIE: the collisional ionization model with the mass distribution described in Section 2.4. In this section, we show our main results for these models on the gaseous halo mass and the ion column density.

3.1. Fiducial Galaxies

There are four factors affecting the properties of the gaseous halo in our simplified models – the metallicity (Z), the specific star formation rate (sSFR defined as SFR/M_*), the slope of the β -model (β) and the redshift (z). Based on these four dimensions, we have fiducial galaxies defining as $\log M_h = 10.5 - 13.3$, $Z = 0.3 Z_\odot$ (cosmic metallicity), $\text{sSFR} = 10^{-10} \text{ yr}^{-1}$ (star-forming), $\beta = 0.5$ (hydrostatic equilibrium structure) and $z = 0$. For each modeled gaseous halo, we calculate the gaseous halo mass enclosed in the radius range of 5 kpc to the virial radius, and the cooling radius. The calculation results are shown in the Fig. 3.

For the fiducial case, all three models have masses of gaseous halos that are smaller than corresponding stellar masses around the (sub-) L^* galaxies. The largest difference of ≈ 0.5 dex occurs at sub- L^* galaxies ($M_h \approx 4 \times 10^{11} M_\odot$). Overall, the CIE model shows convergence with TCIE in the low-mass region and converges with PIE for massive galaxies. With the halo mass decreasing, the temperature range for TCIE (with $T_{\text{min}} = 3 \times 10^4$) is also decreasing, which leads to the similarity with CIE. Both of collisional ionization models have lower mass gaseous halos than the PIE model because they have a higher radiative emissivity in the low temperature, and the photoionization due to the UVB can support a relatively more massive halo for low-mass galaxies.

In the massive galaxy range, the radiative cooling is reduced at high temperatures, which results in a massive gaseous halo, consistent with theoretical expecta-

tions (Mo et al. 2010). These halos are supported by their buoyancy even for the PIE model. The convergence between CIE and PIE is due to the higher density in massive galaxies – in the inner region (inside of the cooling radius), the average density is higher than 10^{-4} cm^{-3} . This high density corresponds to the low ionization parameter ($U = n_{\text{ph,ionizing}}/n_{\text{H}}$), indicating the weakening of the photoionization. As shown in Fig. 1, the CIE cooling is consistent with the PIE cooling with a density of 10^{-4} cm^{-3} . TCIE has a lower mass gaseous halo than CIE or PIE, due to its higher average emissivity since this model always has low-temperature gas with a higher radiative emissivity.

Overall, the cooling radius varies only modestly over the halo mass range in each model. Specifically, the variation is less than one order of magnitude, and this variation corresponds to the changes in the average emissivity. With the higher emissivity, the cooling radius is larger, however, the changes in the cooling radius is smaller than the emissivity changes. Meanwhile, the cooling radius shows a similar convergence as the gaseous halo mass between CIE and TCIE for low-mass galaxies, and between CIE and PIE for massive galaxies.

3.2. The Effect of Galaxy Properties

By changing the four parameters (Z , sSFR, β and z), we show the effect of these parameters on the resulting hot halo and column densities. For each parameter, we have four choices: the metallicity – $0.1 Z_\odot$, $0.3 Z_\odot$, $1 Z_\odot$, or $2 Z_\odot$; the specific SFR – 10^{-9} yr^{-1} , 10^{-10} yr^{-1} , 10^{-11} yr^{-1} , or 10^{-12} yr^{-1} ; the β parameter – 0.3, 0.4, 0.5, or 0.6; and the redshift – 0, 0.2, 0.5, or 1. In Fig. 4, we show the change corresponding to these parameters as the ratio between varied models and the fiducial model.

The high metallicity increases the cooling emissivity, which reduces the normalization parameter in the β -model, and subsequently the halo mass. With the variation of metallicity in the range $0.1 - 2.0 Z_\odot$, the change of

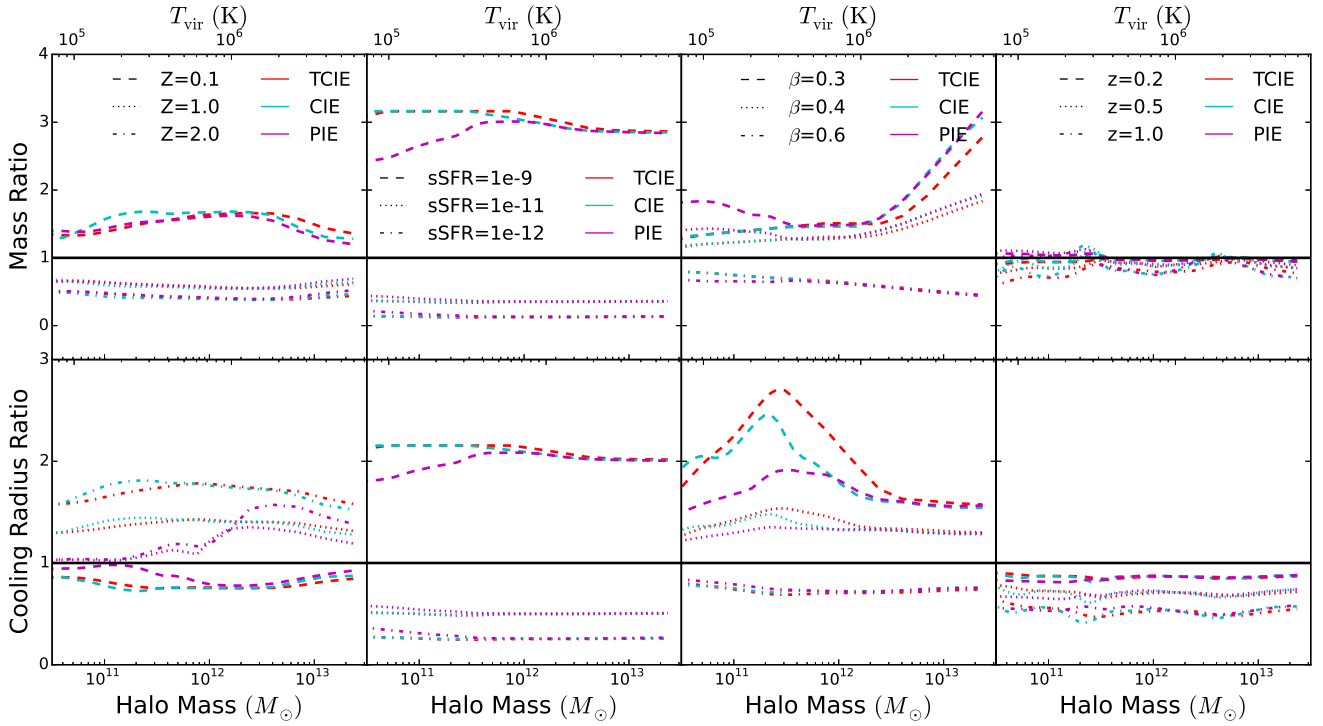


FIG. 4.— Gaseous halo properties as a function of the halo mass for variations in the metallicity (left), the sSFR, the slope of the density profile, and the redshift (right). CIE, PIE and TCIE models are shown in cyan, magenta and red, and the ratios are the values relative to the functional form of the fiducial galaxy has parameters of $Z = 0.3 Z_{\odot}$, $\text{sSFR} = 10^{-10} \text{ yr}^{-1}$, $\beta = 0.5$, and $z = 0$ (in the solid black lines).

the gaseous halo mass is less than a factor of 5, whereas the change of metallicity is a factor of 20. This implies that lower metallicity gaseous halos have a lower total metal mass to account for the same cooling rate. The cooling radius of CIE and TCIE models has a positive dependence on the metallicity due to the increase of emissivity. However, inclusion of photoionization shows a similar cooling radius for different metallicities in the low-mass end, which indicates that the radiative cooling due to the low ionization metal ions is suppressed by the photoionization.

A sSFR of 10^{-11} yr^{-1} is used as a boundary between a star-forming galaxy and a quiescent galaxy, while normal star-forming galaxies have sSFR around 10^{-10} (Renzini & Peng 2015). By increasing the sSFR, the total radiative cooling rate is increased, which means that a massive gaseous halo is needed. For CIE and TCIE, this effect is almost a constant over all mass regions, and PIE shows a similar tendency in the high mass region ($> 10^{12} M_{\odot}$). However, for low-mass galaxies, PIE models with different sSFR values show a significant convergence of the gaseous halo mass, which indicates the effect of a changing sSFR is not as large as CIE or TCIE. The reason for these phenomena is that there are two ways to increase the radiative cooling rate – higher density or higher emissivity. In CIE and TCIE models, the emissivity cannot be increased when the temperature distribution is fixed. Therefore the only way to raise the cooling rate is by increasing the density, which makes the density proportional to the square root of the sSFR for all halo masses. In the PIE model, the emissivity has a dependence on the density as shown in Fig. 1. Within the

cooling radius, the density is higher than 10^{-4} cm^{-2} , and the PIE cooling curve does not deviate from the CIE cooling curve significantly in the temperature range of $\approx 10^{5.5} - 10^6 \text{ K}$. For galactic gaseous halos with these temperatures ($M_h > 10^{12} M_{\odot}$), the emissivity shows a similar behavior as the CIE models, therefore, the change of the density (and the gaseous halo mass) is also similar to the CIE models. For low-mass galaxies with low-temperature halos, the PIE cooling deviates from the CIE cooling curve significantly since the cooling is suppressed for low ionization state ions. Raising the density decreases the photoionization effect, and increases the emissivity to the value of CIE models. Therefore, in the PIE model, the high density not only increases the cooling rate by the squared dependence on the density itself but also increases the emissivity, which leads to a smaller change in the density to account for the high sSFR.

The variation of the sSFR is equivalent to changing the γ factor with the sSFR unchanged. For an example, $\text{sSFR} = 10^{-9}$ with $\gamma = 1$ is the same model as $\text{sSFR} = 10^{-10}$ but with $\gamma = 0.1$. Therefore, our models show that the gaseous halo mass has a square root dependence on the inverse γ factor.

With a larger β , the gas is more concentrated in the central region (at the same gas mass), which leads to the higher emissivity. Since the mass is linearly dependent on the density, the larger β results in a smaller gaseous halo mass. Due to the concentrated emission, the cooling radius is also decreases as β is increases. The effect of larger β also has a dependence on the halo mass – with a more massive halo, the ratio of masses is larger, as shown in Fig. 4. This correlation occurs because the massive

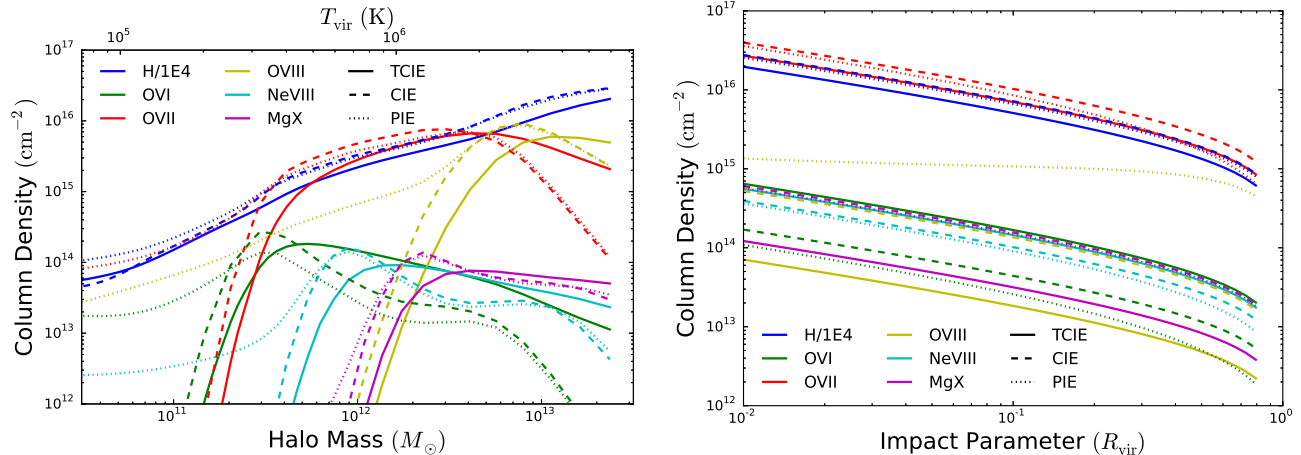


FIG. 5.— Comparison of the ion column density between three models, CIE, PIE and TCIE at $z = 0$, which are shown in dashed, dotted and solid lines, respectively. Different ions are shown in different colors: blue – hydrogen (reduced by a factor of 10^4); green – O VI; red – O VII; yellow – O VIII; cyan – Ne VIII; and magenta – Mg X. *Left panel:* The column density dependence on the halo mass. The galaxy sample is the fiducial galaxy locus, and the impact parameter is fixed to $0.3 R_{\text{vir}}$. *Right panel:* The column density dependence on the impact parameter for the galaxy with $M_* = 7 \times 10^{10} M_\odot$, and $\text{SFR} = 3 M_\odot \text{ yr}^{-1}$, $Z = 0.3 Z_\odot$, and $\beta = 0.5$.

galaxy has a relatively small cooling radius compared to the virial radius, and the flat β -model can host more mass in the region out of the cooling radius.

A higher redshift can affect the gaseous halo through three means – the higher gas density, the younger Universe age and the more intense cosmic background. First, due to the Universe expansion, the higher redshift Universe has a higher density, which leads to the smaller virial radius, and hence higher virial temperature. Second, the younger Universe age at the higher redshift determines a shorter cooling timescale, which reduces the cooling radius and the total cooling rate within this radius. Since CIE and TCIE models have no photoionization involved, these two models are only affected by these two factors. The gaseous halo mass has an anti-correlation with the cooling emissivity of the gas, but the emissivity is a result of a competition of two factors – the increasing emissivity due to the higher density and the changing due to virial temperature. Together, these complex effects leads to a small variation of the gaseous halo mass, with small variations reflecting the shape of the cooling curve (i.e., the bump around $T_{\text{vir}} \approx 10^{5.5} \text{ K}$, also the peak of the cooling curve). For the cooling radius, the effect is clear that the higher redshift leads to a smaller cooling radius. The cooling radius of a $z = 0$ galaxy is about 1.5 times larger than the same mass galaxy at $z = 1$ galaxies.

The cosmic background includes two parts – the UVB and the CMB. As stated in Section 2.3, the inverse Compton cooling is negligible in the low-redshift universe ($z < 6$), but the UVB changes the ionization state distribution, leading to the reduced radiative cooling in the low-temperature region. Therefore, for the low-mass galaxies ($M_h \lesssim 10^{11.3} M_\odot$), a more massive gaseous halo is required to account for the same SFR with the UVB increasing at the higher redshift, which results in the mass ratio being slightly larger than 1. For the high-temperature end, the PIE model converges with the CIE model, which is expected.

3.3. The Ion Column Densities

With the calculated density profile and the temperature distribution, we calculate the column density for ions of interests (mainly high ionization state ions), which are more common in the hot ambient medium. For CIE and TCIE models, we adopt the ionization distributions from [Bryans et al. \(2006\)](#), which only has a dependence on the temperature. The PIE ionization fraction is adopted from [Oppenheimer & Schaye \(2013\)](#), which is tabulated based on the redshift, the metallicity, the density and the temperature.

For the TCIE model, we calculate the average ionization fraction using

$$\bar{f}_i = \int_{T_{\text{min}}}^{T_{\text{max}}} f_i(T) M(T) dT. \quad (13)$$

Here, we assume that multi-phase medium has similar covering factors around 1, which implies that the multi-phase medium is well-mixed. This assumption should be good for high ionization state ions. [Werk et al. \(2013\)](#) shows that intermediate ionization ions (i.e., C III, Si III, Si IV) and high ionization ions (i.e., O VI) have comparable covering factors around 0.8, except that O VI seems to be less in quiescent galaxies. However, this is probably caused by quiescent galaxies that are usually massive galaxies with higher virial temperatures ([Oppenheimer et al. 2016](#)).

In Fig. 5, we compare the three models (CIE, TCIE and PIE), showing ion column densities for star-forming galaxies (i.e., $Z = 0.3 Z_\odot$, $z = 0$, $\text{sSFR} = 10^{-10} \text{ yr}^{-1}$ and $\beta = 0.5$). To show the dependence on the stellar mass, we fix the impact parameter to $0.3 R_{\text{vir}}$, which is a typical impact parameter in the COS-Halos program and also leads to a similar column for ions observed in the MW from the Sun. Similar to the result of the gaseous halo mass, CIE and PIE shows the convergence of H I column densities from $M_h = 4 \times 10^{11} M_\odot$ and above, which indicates that the cooling emissivity is almost the same. However, other ions do not show the same similar-

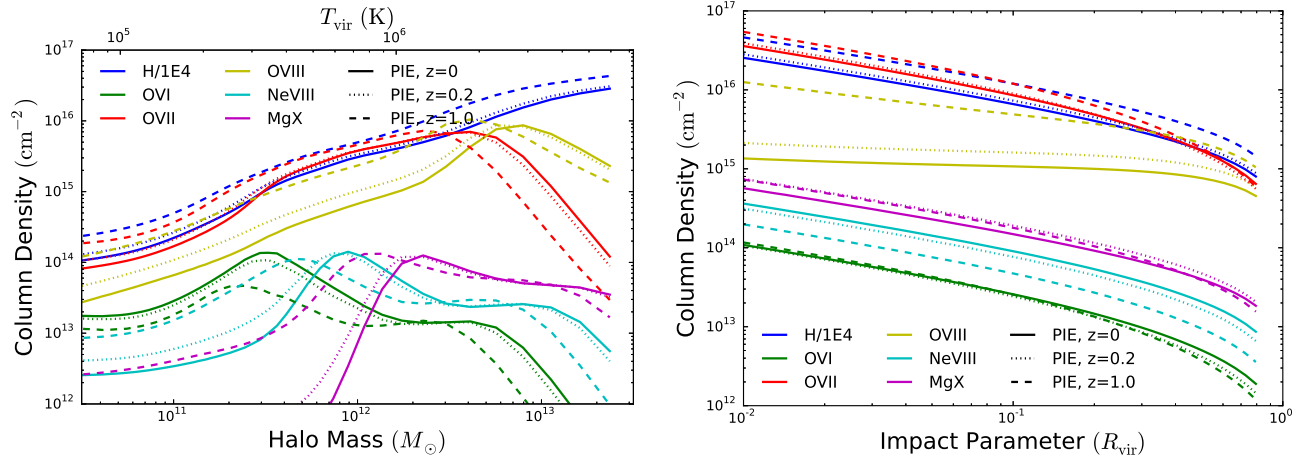


FIG. 6.— Comparison of the ion column density of the PIE model at different redshifts. Ions are encoded in the same colors as Fig. 5, while solid, dotted, and dot-dashed lines are PIE models with $z = 0$, $z = 0.2$, $z = 1.0$, respectively. The galaxy sample configuration is also the same as Fig. 5. *Left panel:* The column density dependence on the halo mass. Since the virial temperature has the dependence on the redshift, the shown T_{vir} is at $z = 0$. *Right panel:* The column density dependence on the impact parameter. The higher redshift leads to a higher virial temperature, and shifts the peaks of ions to lower-mass galaxies. Both the higher virial temperature and more intense UVB increase the higher ionization state ion column densities for higher redshift galaxies.

ity, which indicates that the ionization fractions are not similar. Only the most massive halo ($M_h > 10^{13} M_\odot$) has similar ionization fractions for CIE and PIE due to the relatively higher density. In low-mass galaxies (at the left side of the ionization peak for different ions), PIE leads to extended tails for high ionization state ions (e.g., O VI and O VII) because of the low density.

Compared to CIE or PIE without cooling temperature distributions, TCIE does not show the shape of the ionization fraction function directly, but it shows a flattened peak for high ionization state ions. For O VI and O VII, column density peaks are $\gtrsim 10^{14} \text{ cm}^{-2}$ and $7 \times 10^{15} \text{ cm}^{-2}$, respectively. O VI is higher than $10^{13.5} \text{ cm}^{-2}$ over a halo mass range of $2 \times 10^{11} M_\odot$ to $4 \times 10^{12} M_\odot$. Ne VIII and Mg X show comparable flattened column density distributions in the range of $10^{13.5} - 10^{14.0} \text{ cm}^{-2}$, while Ne VIII occurs in lower mass galaxies compared to Mg X.

To show the ion column density dependence on the impact parameter, we choose a MW-like galaxy with $M_\star = 7 \times 10^{10} M_\odot$, $\text{SFR} = 3 M_\odot \text{ yr}^{-1}$, $Z = 0.3$, $\beta = 0.5$ and $z = 0$. In CIE and TCIE models, the ionization fraction does not have a dependence on the density, so the average ionization fraction has no dependence on the impact parameter. Therefore, all columns follow a general radial decrease of the β -model. For the PIE model, the significant flattening of O VIII in the small impact parameter region shows that the ionization fraction in the inner region is much smaller than the outer region, where the photoionization generates more O VIII (Oppenheimer & Schaye 2013). The turnover point is about the half of the virial radius, where about half of O VIII is produced beyond this radius.

We consider the redshift dependence of the PIE model in Fig. 6, which is otherwise similar to Fig. 5. At higher redshifts, the more intense UVB leads to a stronger tail of high ionization state ions in low-mass galaxies. Also, high ionization ions (e.g., O VIII) show peaks at the lower halo mass for the high redshift galaxy, as the O VIII column density peak moves from $M_h \approx 7 \times 10^{12} M_\odot$ ($z = 0$)

to $M_h \approx 4 \times 10^{12} M_\odot$ ($z = 1$). This is mainly due to the increasing virial temperature at higher redshifts. For these higher virial temperatures, the O VIII column density is no longer flat in the small impact parameter region at $z = 1$, which means that the ionization of O VIII is no longer dominated by the photoionization. Although the high density in the inner region still reduces the ionization fraction of O VIII, a significant amount of O VIII is produced in the inner region through collisional ionization.

3.4. Galaxies with the SFR Main Sequence

Using the relationship between the SFR and the stellar mass (Morselli et al. 2016), we generate a set of galaxies with typical SFR, and calculate the ion column densities, showing the result in Fig. 7. The sSFR has a weak dependence on the stellar mass as $\text{sSFR} \propto M_\star^{-0.28}$, so the changes are modest compared to Fig. 3, where the sSFR is constant for different galaxies. Due to the high sSFR of low-mass galaxies ($M_h < 10^{11} M_\odot$), these galaxies have higher normalization factors in the β -model and gaseous halo masses. The gaseous halo mass at the high-mass end ($M_h \approx 10^{13} M_\odot$) is decreased by a factor of two, due to the small sSFR. The cooling radius has a moderately narrow range of 50 kpc to 200 kpc as a function of the halo mass for a given model. Therefore, the increasing R_{vir} leads to a decrease of the relative cooling radius in units of R_{vir} . Compared to Fig. 3, the cooling radius in the low-mass range is raised until $M_h \approx 10^{11.5} M_\odot$, while it is suppressed for the massive galaxy, corresponding to the change of sSFR. For dwarf galaxies ($M_h \lesssim 5 \times 10^{11} M_\odot$), the entire gaseous halo is radiatively cooling in CIE or TCIE models, while the PIE model always shows the cooling radius smaller than the virial radius.

We also consider the SFR modification on the ion column density, shown in Fig. 8. Due to the more massive gaseous halo of low-mass galaxies, the total hydrogen column density is increased significantly, while high ionization state ions (e.g., O VII and O VIII) changes within

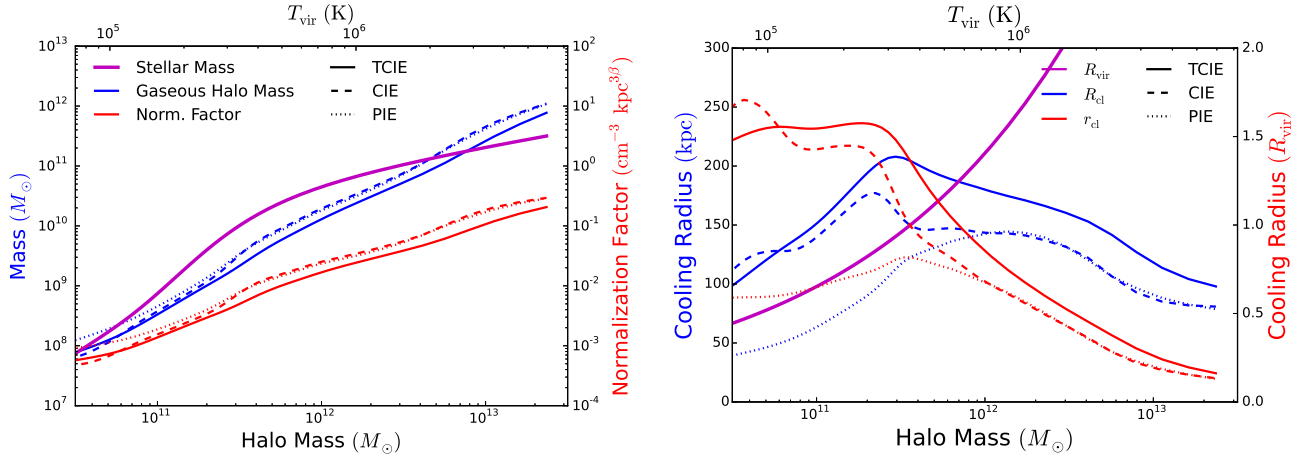


FIG. 7.— The gaseous halo mass and the cooling radius of galaxies where the SFR is given by the mean fundamental plane SFR-stellar mass relationship of [Morselli et al. \(2016\)](#). *Left panel:* The gaseous halo mass and the normalization factor. *Right panel:* The cooling radius dependence on the halo mass. These two plots are encoded in the same way as Fig. 3. The relatively higher sSFR for low-mass galaxies, leads to more massive gaseous halos and larger cooling radius, while massive galaxies have lower mass and smaller cooling radius compared to Fig. 3.

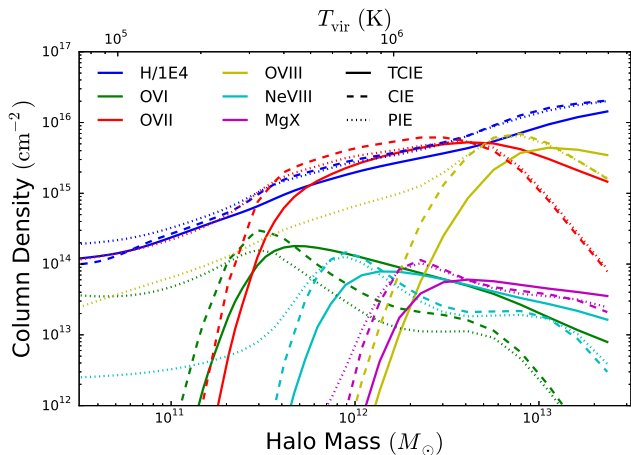


FIG. 8.— The column density dependence on the halo mass of galaxies with fundamental plane SFR. The ion colors are same as Fig. 5. Similar to the comparison between Fig. 7 and Fig. 3, the changing of sSFR leads to higher column densities for low-mass galaxies, and lower column densities for massive galaxies, compared to Fig. 5.

a factor of 1.5. The massive galaxy shows ions with column densities slightly smaller than Fig. 5. Overall, the sSFR dependence on stellar mass does not change the phenomena illustrated by the fixed sSFR models, such as the convergence between models.

4. DISCUSSION

Currently, modeling of gaseous components in halos often assume a single-temperature CIE model or a photon-heated PIE model ([Stocke et al. 2013](#); [Werk et al. 2014](#); [Miller & Bregman 2015](#); [Nicastro et al. 2016a](#); [Faerman et al. 2017](#)). Improvements in such assumptions are warranted by observations that indicate the presence of multi-phase medium and temperature variations over different radii ([Anderson et al. 2016](#); [Tumlinson et al. 2017](#)). However, both of these two temperature issues

are not well constrained observationally – there is not a universal temperature distribution for multi-phase gas or a universal radial-dependence of the temperature ([Anderson et al. 2016](#); [Bogdán et al. 2017](#); [Tumlinson et al. 2017](#)).

Besides the gas temperature, the contribution by photoionization is controversial regarding the effect on high ionization state ions. The photoionization model is employed to explain the low and intermediate ionization state absorption system seen against the UV spectrum of background QSOs ([Werk et al. 2014](#)). High ionization state ions (e.g., O VI and Ne VIII) are normally explained in the collisional ionization model ([Savage et al. 2005](#); [Narayanan et al. 2012](#); [Meiring et al. 2013](#); [Pachat et al. 2017](#)), while they are also possible to be modeled by photoionization ([Hussain et al. 2015, 2017](#)).

In the last decade, the effect of the photoionization and the radiative cooling has been considered in theoretical calculations ([Wiersma et al. 2009](#); [Oppenheimer & Schaye 2013](#); [Gnat 2017](#)). Benefiting from these numerical calculations, we apply two improvements to the modeling of gaseous halos – the photoionization modification and the radiative cooling multi-phase medium. These two improvements change the radiative cooling rate of the gaseous halo, subsequently the mass of the gaseous halo, and ions hosted by the halo. In this section, we compare our models with observations and theoretical simulations, and discuss implications and limitations.

4.1. The Most Applicable Models

In our gaseous halo model, we consider the modification of the photoionization and the effect of the radiatively cooling multi-phase medium, separately. In general, the photoionization mainly affects the low temperature or the low-density regions. In the context of a gaseous halo, the low temperature gas is most common in low-mass galaxies, while the low-density gas is on the outskirts of gaseous halos. Meanwhile, the radiative cooling mainly occurs within the cooling radius, where the density is high enough for the effective radiative cool-

ing. However, these modifications have several limitations, which should be considered when one evaluates the applicability of these models.

For the photoionization of the gaseous halo, there are two main limitations – the lack of ionizing photons from the host galaxy and the lack of the radiation transfer inside the halo. First, we only employ the UVB to supply ionizing photons, however, it is not the only source of the high-energy ionizing photons. The host galaxy also provides ionizing radiation from the star formation or soft X-rays from shock heated gases due to stellar winds and supernovae. Assuming an escape fraction of the unity of soft X-rays, [Suresh et al. \(2017\)](#) show that the impact of the photoionization due to the host galaxy is limited to the inner 50 kpc traced by the O VI. Typically, the escape fraction is only several percent for low-redshift galaxies ($z < 2$; [Grimes et al. 2009](#); [Khaire & Srianand 2015](#)), which indicates that the galaxy escaping ionizing flux dominates the innermost region within the cooling radius. Second, ionizing UVB photons will be diluted by the absorption inside the gaseous halo, which leads to the suppression of the photoionization with the decreasing radius. The decreased photoionization means that the medium in the inner region is more likely to be collisionally ionized. Therefore, the UVB-only PIE model is more likely the case for the outer region of massive halos.

We assume a time-independent cooling model for the multi-phase radiatively cooling medium, where the mass cooling rate is constant over all temperatures. This model has two assumptions – the gases at different temperatures are “well-mixed” and the hot medium can always be supplied to keep the cooling time independent. The first assumption means that the multi-phase ionic structure should have a physical connection (mixture) at various temperatures to keep the same mass cooling rate, and the cooling is only due to the radiative losses of the whole gaseous halo. However, some of the physical aspects surrounding the cooling are still uncertain, which is related to various processes besides the pure radiative cooling – the galactic fountain, the accretion from IGM and even the tidal effect due to nearby galaxies ([Bregman 1980](#); [Kwak & Shelton 2010](#); [Marinacci et al. 2010](#); [Gnat 2017](#)). These processes introduce perturbations to the gaseous halo, which leads to denser regions and possible thermal instabilities that might enhance the radiative cooling ([Armillotta et al. 2016, 2017](#)). These processes cannot be investigated in our analytic model, but might find solutions in the highest resolution cosmological simulations, which is beyond the scope of this paper. However, [Thompson et al. \(2016\)](#) show that the cooling can follow the constant mass cooling rate model in a detailed radiative-cooling hot-wind model with mass-loading and energy transfer. In their calculation, the stable cooling model is evident in the large mass-loading factor $\dot{M}_{\text{hot}}/\text{SFR} \gtrsim 1$ case, which is related to another assumption on the boundary condition.

This boundary condition – an infinite ambient hot medium – is required in a steady state model to balance the cooling rate of the gas. Without this boundary condition, the cooling will reduce the mass and the density of the hot gas, and subsequently reduce the cooling rate in the high temperature region, which violates the constant mass cooling rate assumption. In [Thompson et al.](#)

(2016), the low mass-loading case shows the flattened $dL/d\ln T$ in the high temperature region, indicating the lower cooling rate, which directly results from the weakening of the boundary condition. In the context of our gaseous halo model, this boundary condition could be satisfied automatically when the cooling radius is significantly smaller than the virial radius, which means that the gas beyond the cooling radius can be treated as the ambient hot phase gas to supply the cooling medium.

Based on above discussions, we suggest that gaseous halos should be divided into two categories based on their host galaxy masses. For the low-mass galaxy ($M_h \lesssim 4 \times 10^{11} M_\odot$), the PIE model is a good assumption, since its halo size is small, and the virial temperature is low. For such a gaseous halo, the photoionization must be considered, since it provides additional heating to support a more massive gaseous halo, and changes the distribution of ionization states significantly. Also, low-mass galaxies normally have lower SFR ($\lesssim 1 M_\odot \text{ yr}^{-1}$), which reduces the ionizing flux from the host galaxy, and it is approximately correct to assume the UVB-dominated photoionization. However, one potential issue is that the stellar feedback is stronger with the decreasing halo mass, which implies the feedback heating is higher and the γ factor is smaller in Equation (2). Considering this effect, the low-mass galaxy may host a higher mass halo than the PIE model predicts. Considering the radiative cooling, we could use the TPIE model, which is more realistic, since the cooling radius is smaller than the virial radius as shown in Fig. 7. In the next section, we will show that the photoionization modification on the TCIE model is similar to its effect on the CIE model.

For a high-mass galaxy ($M_h \gtrsim 4 \times 10^{11} M_\odot$), the virial temperature is high ($> 10^{5.5} \text{ K}$) and the cooling radius is smaller than the virial radius. Therefore, we suggest that the whole gaseous halo should be divided into two parts – the inner high-density region within the cooling radius and the outskirts, which is a low-density region. In the inner region, the cooling produces a multi-phase medium, therefore, the TCIE model is preferred. Also, in this case the boundary condition is satisfied to maintain the system in a steady-state. Beyond the cooling radius, the PIE model is appropriated due to the density of $\lesssim 5 \times 10^{-5} \text{ cm}^{-3}$.

4.2. The Multi-Phase Cooling Medium With Photoionization

The TPIE model – the stable radiative cooling model with the photoionization – is a more complex extension of the earlier models, and there are two potential issues with such a model. First, with the effect of photoionization increasing, the gas could be in a net heating phase, which could break our assumption on the stable radiative cooling model. This phenomenon is important where the photoionization might support gaseous components in special situations, such as at 10^4 K and within $\sim 1 \text{ kpc}$ of the plane (as occurs in the Milky Way – the gaseous disk). However, this case is not the aim of our models. Second, the TPIE model leads to a radial dependence in the temperature distribution, since PIE cooling curves have a dependence on the density. This involves the modeling of the cooling flow, which is not included in our models. Meanwhile, as we will show below, the

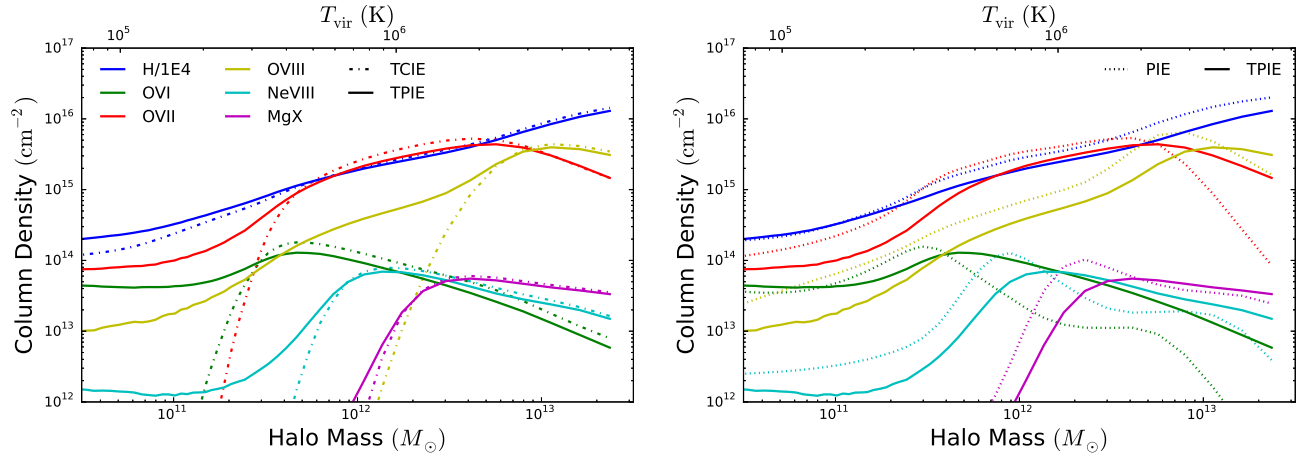


FIG. 9.— The comparison between PIE, TCIE, and TPIE models. Ions have the same colors as in Fig. 5, while solid, dotted and dot-dashed lines are TCIE, PIE, TPIE models, respectively. *Left panel:* We compare the TCIE and TPIE models, which are the most realistic. For T_{vir} values below the peak column densities of the TCIE model, the column is considerably enhanced for the metal ions due to the photoionization modification. *Right panel:* We compare the PIE and TPIE models, where more relatively low ions for massive galaxies (e.g., O VI) is produced due to the cooling of the high temperature medium.

TCIE and PIE models can be a good approximation for the TPIE model in different situations.

In the TPIE model, there are two modifications compared to the previously defined model. First, the lower limit of temperature in TPIE is no longer fixed at $10^{4.5}$ K due to the potential heating. We set a minimum emissivity of 10^{-26} erg $\text{cm}^3 \text{s}^{-1}$ (corresponding to a minimum temperature), which sets a dynamic range of more than three orders of magnitude for the emissivity. If this temperature is higher than $10^{4.5}$ K, then the local minimum temperature is changed to the new temperature with the minimum emissivity. In practice, only few percent of gas has the new lower limit of temperature (about 5×10^4 K to 10^5 K), which is not far from our fixed minimum temperature (3×10^4 K). Second, for different temperatures, the density is also different due to the pressure balance, which leads to different cooling curves. However, this involves radiative transfer to obtain the photon spatial distribution in the gaseous halo. Therefore, we ignore such an effect and use the cooling curve of the total density to calculate the mass-temperature distribution for all different temperatures.

In the calculation of TPIE, we use the galaxy sample with the typical SFR dependence on the stellar mass. Other parameters are fixed, including the metallicity of $Z = 0.3 Z_{\odot}$, redshift of $z = 0$, $\beta = 0.5$, and the impact parameter of $0.3 R_{\text{vir}}$. The results are compared to TCIE and PIE models, as shown in Fig. 9.

The gaseous halo mass is proportional to the normalization factor in the β -model, which is also indicated by the hydrogen column density. For the gaseous halo mass, the TPIE model converges to the TCIE model for massive galaxies ($\gtrsim 10^{12.5} M_{\odot}$), and show similarities with the PIE model (with the shift to the high mass galaxy) for low-mass galaxies ($\lesssim 10^{11.5} M_{\odot}$) as expected. Overall, the TPIE is roughly a direct summation of the effect of the photoionization and the cooling temperature distribution. For massive galaxies, the TCIE model is a good approximation of the TPIE model, which has enhanced

“low” ionization state ions (e.g., O VII from the cooling of O VIII). In the low-mass range, the gaseous halo is mainly dominated by the photoionization, which enriches the high ionization state abundance at low temperatures (e.g., O VI or O VII). Therefore, the TPIE model can be approximated by a combination of PIE and TCIE models for all mass ranges.

4.3. The γ Factor

In our model, we introduce a γ factor in Equation (2) to account for the stellar feedback heating. In the previous calculation, this γ factor is fixed at unity for simplicity. However, the γ factor varies over different galaxies, which is determined by the detailed physics of the stellar feedback – supernovae (SNe), stellar winds, photoionization due to the star light and the radiation pressure (Hopkins et al. 2017). Hopkins et al. (2017) shows that the SN feedback dominates the stellar feedback, although only SN feedback cannot produce observations.

SNe can launch a galactic wind that ejects materials and energy into the gaseous halo or beyond the virial radius (Fielding et al. 2017). The strength of the galactic wind can be modeled by the mass-loading factor η as $\dot{M}_{\text{out}} = \eta \text{SFR}$. The mass-loading factor (at $0.25 R_{\text{vir}}$) has a dependence on the galaxy halo mass (Muratov et al. 2015):

$$\eta = 2.9(1+z)^{1.3} \left(\frac{V_c}{60 \text{ km s}^{-1}} \right)^{-3.2}, \quad V_c \leq 60 \text{ km s}^{-1},$$

$$\eta = 2.9(1+z)^{1.3} \left(\frac{V_c}{60 \text{ km s}^{-1}} \right)^{-1.0}, \quad \text{otherwise}, \quad (14)$$

where V_c is the circular velocity. This is a specific wind model obtained by parametrizing the galactic winds in the FIRE simulations (Hopkins et al. 2014). For the energy carried by the galactic wind, we only consider the kinetic energy, ignoring the internal energy, since the temperature of the galactic wind is found to be much lower than the virial temperature in simulations (Field-

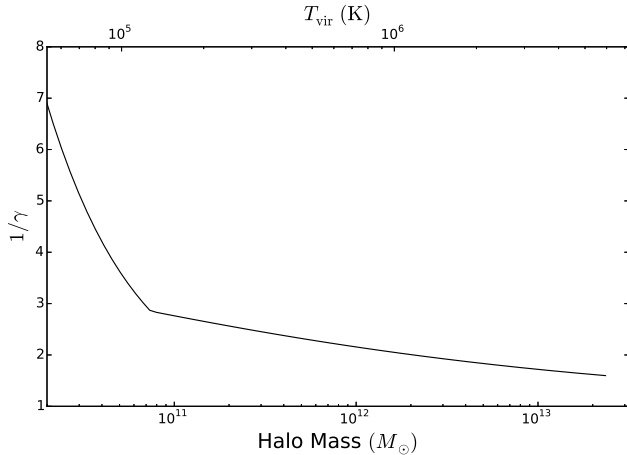


FIG. 10.— The stellar feedback parameter γ as a function of halo mass, where higher $1/\gamma$ indicates stronger stellar feedback heating.

ing et al. 2017). For the wind internal energy, Thompson et al. (2016) showed a semi-analytic model for the cooling wind, and found a drop of the temperature at the radius of 5–10 kpc for high mass-loading cases ($\eta > 0.8$), which agree with Muratov et al. (2015). The wind temperature is only about one tenth of the virial temperature, when it enters the innermost radius in our model. Therefore, the internal energy of the wind is negligible compared to the virial temperature of the halo.

The wind velocity is $V_{\text{wind}} = 0.85V_c^{1.1}$, which is also measured at $0.25 R_{\text{vir}}$ (Muratov et al. 2015). Based on these relationships, we can set an upper limit for the stellar feedback, since not all of the kinetic energy can be converted into the internal energy of the gaseous halo. Some of the galactic wind will be recycled before it is well-mixed with the gaseous halo, and some will be ejected out of the galaxy halo. Therefore, the lower limit of γ factor is calculated by:

$$\frac{1}{\gamma} = 1 + \eta(V_c) \left(\frac{V_{\text{wind}}^2}{V_c^2} - 1 \right), \quad (15)$$

Then, the γ factor is around 0.14 for the lowest mass galaxies, and around 0.5 for galaxies with masses higher than $10^{11} M_{\odot}$. We show the halo mass dependence of γ in Fig. 10.

4.4. The O VI Puzzle

From our models, we find that the O VI column lies in a moderately narrow range close to 10^{14} cm^{-2} for all masses of galaxies due to either the photoionization (in low-mass galaxies) or the low-temperature cooling medium (in massive galaxies; Fig. 11). Current observations show that the O VI has a significant dependence on the star formation rather than the stellar mass (Tumlinson et al. 2011), which seems to be reproduced by the TPIE model. Therefore, we compared the prediction from our models with observations, and we adopt three samples – COS-Halos (Werk et al. 2013), Johnson et al. (2015) and Johnson et al. (2017). Our models have the parameters $Z = 0.3 Z_{\odot}$, $\beta = 0.5$ and the SFR is from the main-sequence relationship (also modified using redshift; $\text{sSFR} \propto (1+z)^3$). The impact pa-

rameters of $0.3 R_{\text{vir}}$ and $0.6 R_{\text{vir}}$ are shown since the COS-Halos sample is limited to $< 0.55 R_{\text{vir}}$. The redshift is set to 0.2 since most of the O VI samples have $\bar{z} \approx 0.2$. As shown in Fig. 11, the TPIE model can be approximated by the combination of PIE and TCIE with a broad transition around $M_h \approx 3 \times 10^{11} M_{\odot}$. Therefore, in the following discussion, the TPIE designation represents the combination of PIE and TCIE models. For low-mass galaxies ($M_h \lesssim 3 \times 10^{11} M_{\odot}$), the O VI is mainly ionized through photoionization for the whole gaseous halo, while for the higher mass galaxies, the cooling medium corresponds to the majority of observed O VI. The TPIE model predicts a narrow range of column densities from $M_h = 3 \times 10^{10} M_{\odot}$ to $2 \times 10^{13} M_{\odot}$. In most mass regions, the TPIE model predicts an O VI column density of $10^{13.5} \text{ cm}^{-2}$ to $10^{14.1} \text{ cm}^{-2}$.

For the COS-Halos sample, the line shape of O VI usually shows multiple components, which can be separated by using the Voigt profile fitting. However, in addition to component separation, there is the issue of the host galaxy. Werk et al. (2013) assigned one galaxy for each multi-component absorption system and calculated the SFR. Therefore, we adopt their measurements based on the apparent optical depth method, which does not separate different components. One caveat is that this treatment of different components might give higher O VI column densities than the isolated gaseous halo. Several galaxies in the COS-Halos sample have other lower mass galaxies at the same redshift in the same field or lie in galaxy groups, which may introduce contamination from the other galaxies or from the intragroup medium. Since the COS-Halos sample also provides the SFR for each galaxy, we mark with blue a galaxy that has a SFR higher than the SFR calculated from the SFR main sequence, while a lower one is red. For galaxies with non-detections of O VI, we set the upper limit as the detection limit if it is available.

The Johnson 2015 sample considered galaxies in groups or clusters with isolated galaxies, so we used only isolated galaxies with impact parameters smaller than the virial radius. Johnson et al. (2015) do not have information on the SFR, but they report the galaxy type. Therefore, we assign early-type galaxies with red colors and late-type galaxies with blue colors. This color encoding is different from the COS-Halos sample, but will not affect the general tendency. The Johnson 2017 sample focuses on dwarf galaxies with stellar masses in $\log M_* = 7.7 - 9.2$ (Johnson et al. 2017). For these galaxies, no color is assigned, since no SFR information is available.

In Fig. 11, most of the detected O VI have column densities of $\gtrsim 10^{14} \text{ cm}^{-2}$, no matter whether the SFR is above or below the typical SFR. Overall, the difference is about 0.3–0.5 dex, which may be accounted for by two explanations. One is the heating from the stellar feedback, which might produce a smaller γ factor in Equation (2). A factor of 4 to 10 can raise the normalization factor in the β -model by a factor of 2 to 3, which also raises the O VI column density by the same ratio. Similarly, McQuinn & Werk (2018) showed that a cooling flow with $100 M_{\odot} \text{ yr}^{-1}$ can account for the observed O VI column density, and that most of the cooling flow might be destroyed by stellar feedback. However, the galactic wind only feedback model is unlikely to be sufficiently en-

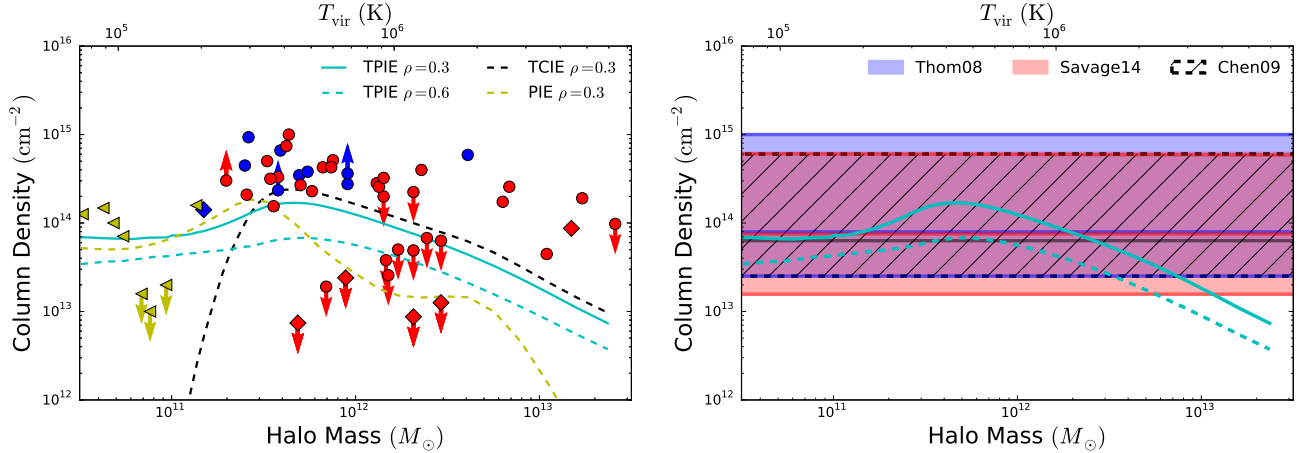


FIG. 11.— Comparison of OVI columns in our models and observations. *Left panel:* Comparison with O VI-galaxy pairs. The cyan lines are the TPIE model, and the solid line has an impact parameter of $0.3 R_{\text{vir}}$, while the dashed cyan line is $0.6 R_{\text{vir}}$; most observations fall between these two impact parameters. The black dashed line is the TCIE model with an impact parameter of $0.3 R_{\text{vir}}$, while the yellow dashed line is PIE model with the same impact parameter. The filled circle marks the O VI column in [Werk et al. \(2013\)](#), and the red color indicates that the SFR is lower than the typical SFR, while the blue color indicates higher SFR values. The upper limit for column density is the detection threshold. The sample of [Johnson et al. \(2015\)](#) is shown by diamond symbols, and the color indicates whether the galaxy is early-type (red) or late-type (blue). The sample of [Johnson et al. \(2017\)](#) is shown in yellow left triangles. The COS-Halos sample lies about 0.5dex over our models. *Right panel:* Comparison with blind O VI surveys. Three samples are marked in blue, black slashed, and red slashed regions for [Thom & Chen \(2008\)](#), [Chen & Mulchaey \(2009\)](#), and [Savage et al. \(2014\)](#), respectively. The median value for these samples are shown in corresponding solid lines, which are consistent with our models.

ergetic based on our calculation in Section 4.3. Another possibility is that the observed O VI is overestimated due to the intragroup medium contamination or the overlap of multiple gaseous halos in the sightline ([Stocke et al. 2014](#)).

To address this possibility further, we do not limit the sample to O VI-galaxy pairs, but also consider all intervening O VI absorption systems from blind surveys. We consider three samples – [Thom & Chen \(2008\)](#), [Chen & Mulchaey \(2009\)](#), and [Savage et al. \(2014\)](#). These three samples have some overlap with each other, but since the detection methods are not the same, they are also complementary to each other. In [Thom & Chen \(2008\)](#), the median O VI column density is $\log N(\text{OVI}) = 13.9$ with a standard deviation of 0.4 dex, while in [Chen & Mulchaey \(2009\)](#), the O VI column density has a median value of $\log N(\text{OVI}) = 13.8$ and a scatter of 0.4 dex. In [Savage et al. \(2014\)](#), the components are reported separately. The median column density of single O VI components is $\log N(\text{OVI}) = 13.68$ with a range of 13.00 to 14.59. The average number of components per O VI absorption system is around 1.6, which leads to the average O VI column density for each O VI system of $\log N(\text{OVI}) = 13.87$. These three surveys are consistent with each other in terms of the median and range of $N(\text{OVI})$.

Although these intervening O VI systems currently do not have detected host galaxies, it is possible that they are also the gaseous halo of galaxies, whose luminosities are below $0.1 L^*$ ($M_h < 3 \times 10^{11} M_\odot$; the detection limit of the COS-Halos galaxy sample). If this is the case, these O VI observations show a significant difference from the COS-Halos sample, whose median is $\log N(\text{OVI}) = 14.5$ with a scatter of 0.26 dex (only accounting for the detected O VI).

Since the COS-Halos sample provides the SFR for each O VI-galaxy pair, we built a specific model (with γ) for

individual systems based on its stellar mass, SFR, and impact parameter from [Werk et al. \(2014\)](#). We only use the physical impact parameter from the COS-Halos sample, and we recalculate the relative impact parameter using R_{vir} calculated from Equation (3) with a mean halo density of $200\rho_{\text{crit}}$ rather than $200\rho_{\text{matter}}$. These recalculated virial radii are smaller than those presented in [Werk et al. \(2014\)](#) by a factor of $\approx 30 - 40\%$ within the redshift range of $z = 0.14 - 0.36$. This modification leads to larger relative impact parameters. For the QSO-galaxy pair J1437+5045 and 317_38 (here we use the same notation of COS-Halos sample – position angle and angular separation), our calculation leads to the virial radius of 140.2 kpc, which indicates that the absorption system is beyond the virial radius at $z = 0.246$ with the impact parameter of 143 kpc. Although different stellar mass-halo mass relationships and different cosmological constants can lead to different results on the virial radius, the systems with reported $\rho/R_{\text{vir}} > 0.5$ are actually further out in the halo ($\rho/R_{\text{vir}} > 0.8$).

Our calculations for the O VI column density are shown in Fig. 12. If the SFR of a galaxy is the upper limit, we can only derive the upper limit of the O VI column density. Among 30 systems with detectable O VI, there are five that do not have measurable SFRs. It is clear that some of these five systems are in galaxy groups – the galaxy 211.33 of QSO J1133+0327 has a similar redshift ($\Delta z < 0.0002$) to the galaxy 110.5 adopted in the COS-Halos study, and the galaxy 35.14 of QSO J0910+1014 has the similar redshift of the galaxy 242.34. For these O VI absorption systems, it is possible that they are due to the intragroup medium or smaller galaxies that are closer, since we have shown that the O VI column density can be detected for low-mass galaxies ($M_h < 3 \times 10^{11} M_\odot$), which is consistent with observations ([Johnson et al. 2017](#)). Such contamination may also explain

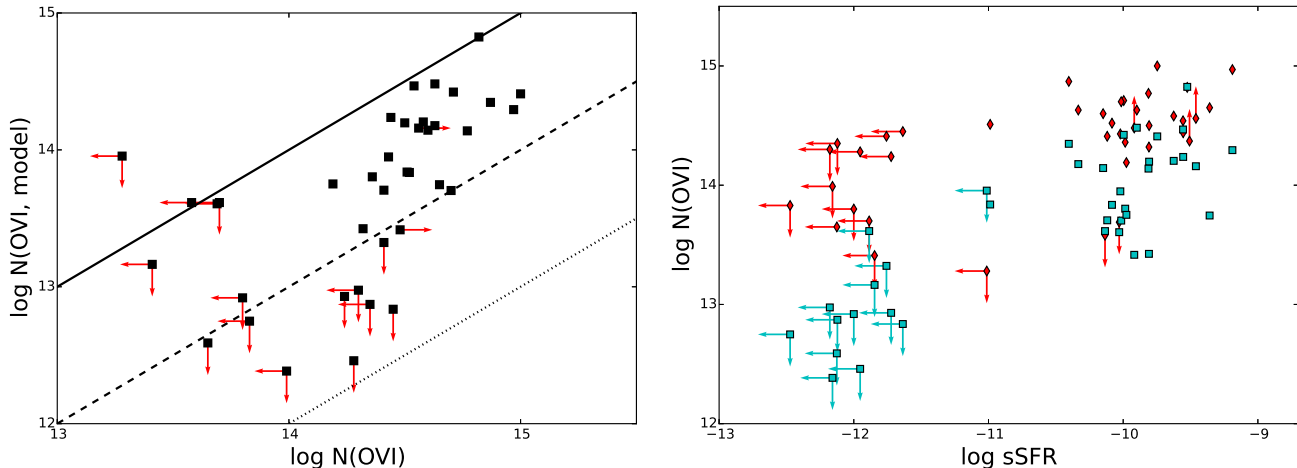


FIG. 12.— Specific models for the COS-Halos O VI sample. *Left panel:* For each system, the predicted O VI column density is calculated with the reported stellar mass, the SFR, and the impact parameter. If the SFR is only an upper limit, then our models predict an upper limit. The solid, dashed, and dotted lines indicate models are equal to observations, 10%, and 1% of observations. For detected objects, the model are typically a factor of 3 – 5 lower than the observations, which is consistent with Fig. 11. *Right panel:* The sSFR dependence of the O VI column density. The red diamonds are the observations, while the cyan squares are our models.

some of the difference between the model and the observation. As shown in Bregman et al. (2018), there are two small galaxies surrounding QSO J1009+0713 with a redshift of 0.3556 similar to the galaxy 170.9 (0.3557). For this system, the O VI has four components, which have velocities of -95 km s^{-1} , 25 km s^{-1} , 117.2 km s^{-1} , and 200.7 km s^{-1} . For the galaxy 170.9, our model predicts $\log N(\text{OVI}) = 14.41$, while the two components of two high velocities are 14.21 ± 0.16 and 14.34 ± 0.05 , respectively. The two components at low velocities are larger contributors (14.61 ± 0.05 and 14.52 ± 0.12) to the total O VI column density of 15.00 ± 0.03 , and we suggest that they may be associated with the two small galaxies with slightly lower redshifts. Overall, our specific models show a difference of 0.5 dex smaller than the detected O VI from COS-Halos, which is similar to our general comparison shown in Fig. 11.

In Fig. 12, we also show the relationship between the sSFR and the O VI column density. Our models show results similar to the Evolution and Assembly of GaLaxies and their Environments (EAGLE) simulation (Oppenheimer et al. 2016). For star-forming galaxies, the predicted O VI column densities are about 0.5 dex lower than the observation, while we predict lower O VI column densities for passive galaxies (our upper limit is lower than those simulated in EAGLE; Oppenheimer et al. 2016). The difference for passive galaxies may be due to the lack of AGN heating in our models. The AGN feedback is also proposed to explain the strong O VI in star forming galaxies (Oppenheimer et al. 2017), but as discussed above, this difference is possibly due to contamination in COS-Halos sample.

4.5. The Galactic O VII/O VIII

The O VII and O VIII ions have resonant lines in the X-ray band at 21.60 \AA and 18.97 \AA . However, the detection of these two ions is limited by the current X-ray observatory sensitivity, and only O VII and O VIII in the Milky Way have been confirmed in both absorption and emission (Nicastro et al. 2002; Wang

et al. 2005; Henley & Shelton 2012). The modeling of the O VII and O VIII emission lines shows that the gaseous halo of the MW has a normalization parameter of $1.35 \pm 0.24 \times 10^{-2}/Z \text{ cm}^{-3} \text{ kpc}^{-1.5}$ (Miller & Bregman 2015). For the MW model, we adopt $M_{\star} = 7 \times 10^{10} M_{\odot}$, $M_{\text{h}} = 1.7 \times 10^{12} M_{\odot}$, $Z = 0.3 Z_{\odot}$ and a SFR of $1 M_{\odot} \text{ yr}^{-1}$. This MW model leads to a normalization parameter of $1.75 \times 10^{-2} \text{ cm}^{-3} \text{ kpc}^{-1.5}$, $1.62 \times 10^{-2} \text{ cm}^{-3} \text{ kpc}^{-1.5}$, $1.24 \times 10^{-2} \text{ cm}^{-3} \text{ kpc}^{-1.5}$ and $1.15 \times 10^{-2} \text{ cm}^{-3} \text{ kpc}^{-1.5}$ for the CIE, PIE, TCIE and TPIE models, respectively. For a distance to the galactic center of 8 kpc, the sightline with the galactic latitude of 90° has a column density that is half of the sightline with an impact parameter of $0.03 R_{\text{vir}}$ (8 kpc). Then, the predicted column density is $\log N(\text{OVII}) = 15.6, 15.7, 15.8, 15.6$ for CIE, PIE, TCIE and TPIE, respectively. These column densities lead to an EW of 12 m\AA ($\log N(\text{OVII}) = 15.7$), which is less than the most of the observations as summarized in Hodges-Kluck et al. (2016), where the mean in this direction ($b > 60^{\circ}$) is about 25 m\AA . The corresponding O VIII column densities are 13.9, 14.7, 13.0 and 14.4 for our four models, which is about one order of magnitude lower than observations (Gupta et al. 2012). These modelings show two issues – the ratio of $N(\text{OVIII})/N(\text{OVII})$ is too low and the total amount of oxygen is less than the observation.

For the $N(\text{OVIII})/N(\text{OVII})$ ratio, there are two ways of improving the agreement with Galactic observations – raising the maximum temperature or extending the gaseous halo beyond the virial radius. First, for a $M_{\text{h}} = 1.7 \times 10^{12} M_{\odot}$ halo, the virial temperature is around 10^6 K , while the measured hot gas temperature is around $1.5\text{--}2 \times 10^6 \text{ K}$ (Henley & Shelton 2012; Miller & Bregman 2015; Nevalainen et al. 2017). Also, it is evident that the hot gas temperature is higher than the virial temperature for most elliptical galaxies (Davis & White 1996; Brown & Bregman 1998; Goulding et al. 2016). This higher temperature can increase the $N(\text{OVIII})/N(\text{OVII})$ ratio significantly, since the O VIII ion traces the higher tempera-

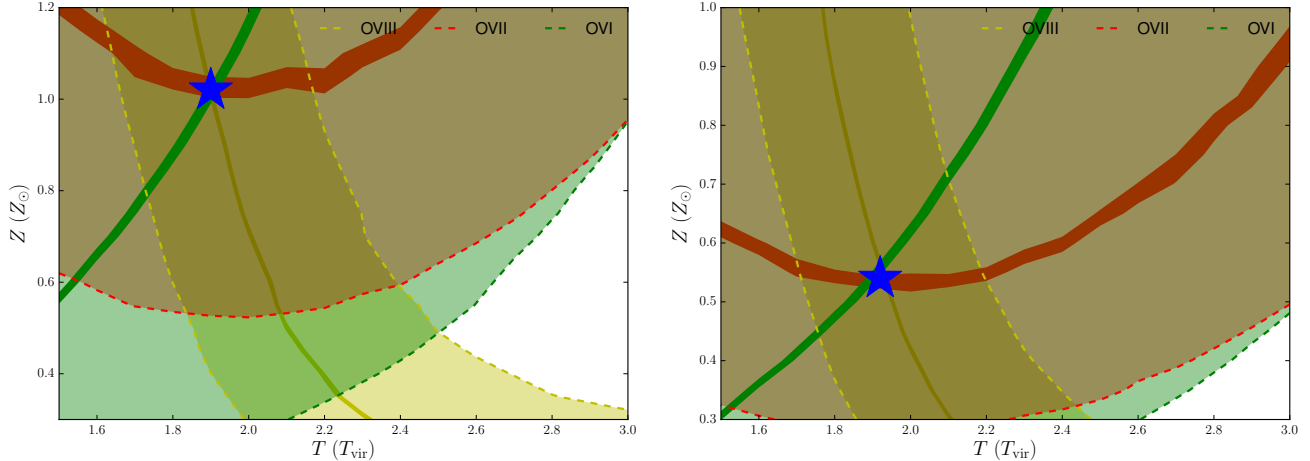


FIG. 13.— Modified model for Galactic O VII and O VIII, constrained by observations, as a function of metallicity and temperature. *Left panel:* Models with the nominal value for γ ($= 1$). The dashed lines indicate the acceptable region for each ion within 1σ . O VIII, O VII, and O VI are in yellow, red, and green, respectively. The thick colored lines indicates the median value of different ions. The blue star indicates the preferred solution with $T \approx 1.90 \times 10^6$ K and $Z = 1.02 Z_{\odot}$. *Right panel:* Models with enhanced stellar feedback ($\gamma = 0.5$), as given in Fig. 10. The symbols are the same as the left panel, but the preferred solution is $T \approx 1.93 \times 10^6$ K and $Z = 0.55 Z_{\odot}$.

ture gas. Second, an extended gaseous halo also changes this ratio involving the photoionization modification as shown in the Section 3.3. Therefore, increasing the maximum radius helps to increase the $N(\text{OVIII})/N(\text{OVII})$ ratio.

To increase the total amount of the oxygen, there are also two approaches – having an extended gaseous halo and increasing the metallicity. For the MW, the cooling radius is smaller than the virial radius, which means that the larger maximum radius will not reduce the normalization factor in the β -model, so this modification only increases the gaseous component surrounding the galaxy, hence the metal mass. As stated in Section 3.2, for a given galaxy-gaseous halo pair (fixed the SFR and the halo mass), higher metallicity leads to a higher total metal mass, although the gaseous halo mass is reduced. Therefore, a higher solar metallicity halo can solve the problem of the small O VII column density in our model.

To illustrate these possibilities, we construct a TPIE model to match the galactic O VII and O VIII observations. In the modified model, we vary two parameters – the maximum temperature $T_{\text{max}} = \alpha T_{\text{vir}}$ and the metallicity. We use the observation summarized in Faerman et al. (2017), which has $N(\text{OVII}) = 1.4(1.0 - 2.0) \times 10^{16} \text{ cm}^{-2}$ and $N(\text{OVIII}) = 0.36(0.22 - 0.57) \times 10^{16} \text{ cm}^{-2}$ (also see Gupta et al. 2012; Fang et al. 2015). The O VI is also considered to show whether it can be reproduced in the same model, and the column density of halo O VI is $\log N(\text{OVI}) = 13.95 \pm 0.34$ (Sembach et al. 2003). For the O VI column density, the contribution from the disk is excluded based on the velocity criterion (Savage et al. 2003).

In Fig. 13, we explore the parameter space of $\alpha = 1.5 - 3$ and $Z = 0.3 - 1.2 Z_{\odot}$, which is determined by the $N(\text{OVIII})/N(\text{OVII})$ ratio and column densities. The acceptable region for each ion is constrained by the observational limits, therefore, the overlap region indicates the preferred parameter space, while the cross of lines indicates the preferred model. Our modified model suggests a super-solar metallicity of $1.02 Z_{\odot}$ and a maxi-

imum temperature of 1.9×10^6 K. This high metallicity solution is not favored since it is very unlikely for the gaseous halo to have higher metallicity than the galaxy disk. This high metallicity is caused by the high oxygen column density in the observation, which can be solved when the γ factor is considered.

Involving the γ factor in Equation (2) can lead to a higher mass gaseous halo, since a $\gamma < 1$ leads to a higher radiative cooling rate. The typical γ factor for the MW is around 0.5. Applying this modification to our model, we will obtain lower metallicity solutions, since the small γ factor leads to a more massive gaseous halo and more metals. Then it is not necessary to have high metallicities to account for observed oxygen. We obtain the best model of the MW gaseous halo with the metallicity of $0.55 Z_{\odot}$ and the maximum temperature of 1.9×10^6 K, showing column densities of $\log N = 13.95, 16.15$ and 15.53 for O VI, O VII, and O VIII ions, respectively. The normalization factor of the β -model is $1.91 \times 10^{-2} \text{ cm}^{-3} \text{ kpc}^{3\beta}$, and the gaseous halo mass is $1.94 \times 10^{10} M_{\odot}$, which contributes 7% to the total baryon mass. The emission line studies of O VII show a normalization factor of $3.39_{-0.55}^{+0.67} \times 10^{-2} \text{ cm}^{-3} \text{ kpc}^{3\beta}$ with $0.3 Z_{\odot}$ (Li & Bregman 2017), which is equivalent to $1.85 \times 10^{-2} \text{ cm}^{-3} \text{ kpc}^{3\beta}$ with $0.55 Z_{\odot}$. Therefore, our MW gaseous halo solution also matches with the emission line study.

We now consider the magnitude of column density increases when the gaseous halo is extended beyond the virial radius. Assuming the maximum radius is twice the virial radius, the change in the column density is about 5% to 8%, which is not enough to account for the observed O VII and O VIII column density. Therefore, compared to the heating due to the stellar feedback, extending of the maximum radius is a secondary effect for the column density, although it leads to a significant increase in the mass, which will be discussed in Section 4.7.

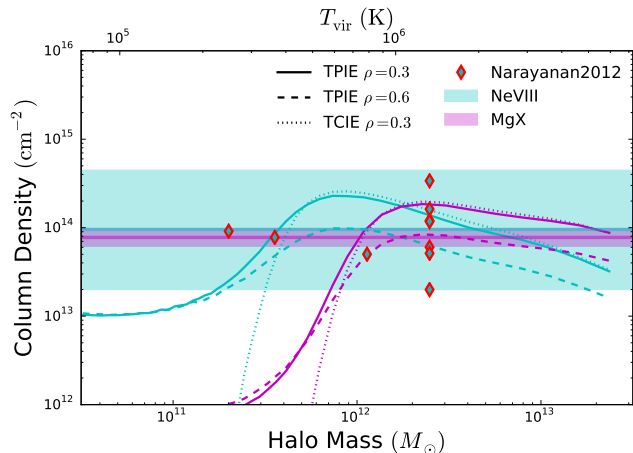


FIG. 14.— Comparison of Ne VIII (cyan) and Mg X (magenta) in our models and observations. The solid, dashed, and dotted lines are the TPIE model with impact parameters of $0.3 R_{\text{vir}}$, $0.6 R_{\text{vir}}$, and the TCIE model with $0.3 R_{\text{vir}}$. The Ne VIII-galaxy pair data is from Narayanan et al. (2012), while the Ne VIII absorption in PG 1206+459 is broken into seven components, and it is not clear which one corresponds to the reported galaxy (Tripp et al. 2011).

4.6. Intervening Ne VIII/Mg X Systems

The Ne VIII and Mg X occurs in the extreme UV band (770 Å and 610 Å respectively), which can only be detected for extragalactic galaxies due to the wavelength limit of Galactic absorption (912 Å) and due to the UV observing band of *HST*/COS (1150 – 1750 Å). The Ne VIII is detectable in the redshift of 0.5 to 1.3, while the Mg X is detectable between $z = 0.9$ and 1.8. At higher redshift, galaxies have a higher mean sSFR, which results in a more massive gaseous halo. In the redshift range of $z = 0.7$ to $z = 1.2$, the SFR is raised by a factor of 5 – 10, which makes the gaseous halo 2 – 3 times more massive, with a similar increase in the column density of Ne VIII and Mg X. In Fig. 14, we show our models of the Ne VIII and Mg X columns at the redshift of 1.

As summarized in Pachat et al. (2017), the median of the detected Ne VIII is $\log N(\text{NeVIII}) = 13.98 \pm 0.31$, varying in the range of $\log N(\text{NeVIII}) = 13.30$ to 14.65. The observed Ne VIII column density shows consistency with our model in a wide galaxy mass range. For the host galaxy, current observations show it varies from $0.08 L^*$ to $\approx 2 L^*$ (Narayanan et al. 2012 and reference herein), which is also well matched with our models. For MgX, there is only one detection towards LBQS 1435-0134, with the column density of $\log N(\text{MgX}) = 13.89 \pm 0.10$ (Qu & Bregman 2016), which is also consistent with the model for a (sub-) L^* galaxy.

The Mg X system in LBQS 1435-0134 is a good example to study the multi-phase medium in the gaseous halo since it has a wide ionization state coverage (i.e., from O III to Mg X), and most of them are high ionization state ions (higher than O IV). In Qu & Bregman (2016), it is modeled by a three-temperature CIE model or a power law model of the column density-temperature distribution with an index of 1.55. This power law model has a total χ^2 of 3.3 with 7 degrees of freedom. We notice the power law index is approximately the slope of the mass-temperature distribution $M(T)$ in the cool-

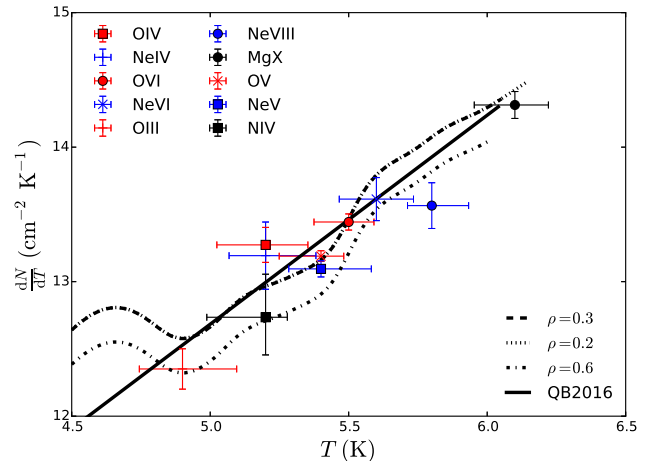


FIG. 15.— The fitting result of TCIE for the Mg X system in the sightline towards LBQS 1435-0134 (Qu & Bregman 2016). For each ion, the temperature is the peak temperature of the ionization fraction, and the error bar is the full width of the half maximum, while the y axis value is the normalized column density gradient, which is given by $\frac{dN_{\text{H,ion}}}{dT} = \frac{dN_{\text{H,model}}}{dT} \times N_{\text{ion,observed}}/N_{\text{ion,model}}$. The solid line is the power law model in Qu & Bregman (2016), while dashed, dotted, dash-dotted lines are stable cooling models with impact parameters of $0.3 R_{\text{vir}}$, $0.2 R_{\text{vir}}$, and $0.6 R_{\text{vir}}$, respectively. Note that the $\rho = 0.2 R_{\text{vir}}$ line overlaps with the $\rho = 0.3 R_{\text{vir}}$ line. Therefore, it is clear that the observed power law column density distribution is actually a result of the cooling medium.

ing model, therefore we fit this Mg X system using the TCIE model. The only one variable is the stellar mass, and the SFR is calculated based on the stellar mass and modified by the redshift of 1.2. We use three different impact parameters of 0.2, 0.3 and 0.6. The fitting results are $\log M_* = 10.76$ ($\log M_{\text{h}} = 12.1$) with total $\chi^2 = 65.7$ ($dof = 10$), 10.64 (12.0) with $\chi^2 = 30.0$ (10) and 10.56 (11.9) with $\chi^2 = 131.1$ (10), respectively. Therefore, the Mg X system is likely to be a (sub-) L^* galaxy at the redshift of 1.2. For the best model with $\rho = 0.3 R_{\text{vir}}$, the most of χ^2 (22.0/30.0) is from three ions H I, O IV and Ne VIII. These deviations may be caused by the uncertainty in the lower and the upper limits of the temperature distribution. Extending the lower limit can increase the low and intermediate ionization state ions, while extending the upper limit can decrease the Ne VIII column density as shown in Fig. 14 regarding the $\log M_{\text{h}} = 12.0$. Therefore, although the best reduced χ^2 is around 3, it is a valuable step in modeling such a complex object (the gaseous halo) with a simple physical model.

4.7. Mass Budget

The galaxy missing baryon problem is a crucial aspect of both observation and theory for galaxy formation and evolution, so we also check whether our gaseous halo model can address this issue. In Fig. 16, we show the baryonic fraction for models considered for typical star-forming galaxies. In all mass regions, the cosmic baryonic fraction is significantly higher than the total baryonic fraction of galaxies, which indicates that the gaseous halo within the virial radius cannot account for missing baryons of galaxies in the mass region considered. The overall tendency shows that the low-mass galaxy is more

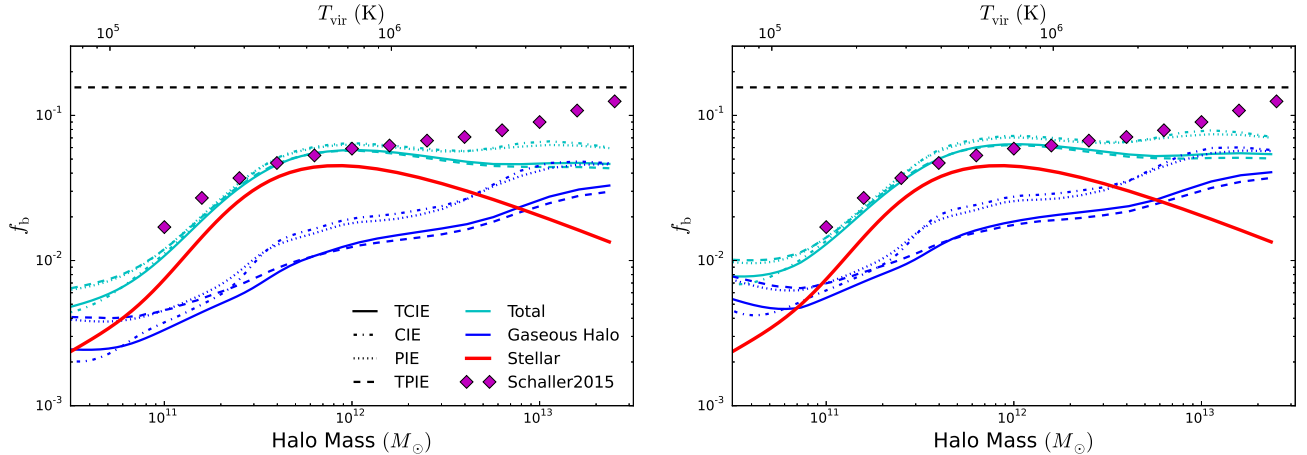


FIG. 16.— The baryonic fraction dependence on the halo mass. *Left panel:* The CIE, PIE, TCIE and TPIE models are shown in dot-dashed, dotted, solid and dashed lines, while the black dashed line is the cosmic baryonic fraction, and the red solid line is the stellar content baryonic contribution. Blue lines are the gaseous-halo-only baryonic fraction, while cyan lines are the total baryonic fraction enclosed in the virial radius. The magenta diamonds are the baryonic fraction from the EAGLE simulation (Schaller et al. 2015). *Right panel:* The baryonic fraction due to the gaseous halo is increased for the enhanced stellar feedback given in Fig. 10. The largest increases occur at lower masses and points at which the stellar and gaseous halos are equal occur at $M_h = 6 \times 10^{10} M_\odot$ for the TPIE model.

baryon-poor than the massive galaxy, showing a sharp rise between $M_h \sim 10^{11} M_\odot$ and $4 \times 10^{11} M_\odot$. The baryonic fraction is almost a constant $f_b \approx 0.05 - 0.06$ for galaxies with higher masses than $5 \times 10^{11} M_\odot$.

These baryonic fractions are the median values for galaxies at different masses, while it is possible to have significant scatter due to the SFR scatter. With the SFR scatter of 0.4 dex (Renzini & Peng 2015), the baryonic fraction could have a scatter of 0.2 dex based on the square root relationship between the sSFR and the gaseous halo mass. This scatter is consistent with cosmological simulations, which shows the baryonic fraction can vary between 20% to 100% of the cosmic baryonic fraction (Marinacci et al. 2014; Muratov et al. 2015; Schaller et al. 2015; Suresh et al. 2017).

That low-mass galaxies have a low f_b is the direct result of both low stellar mass and the high cooling rate. Although they have a relatively high sSFR, the gaseous halo is still low mass and comparable to the stellar mass within a factor of 2. This tendency is consistent with the simulation effort (EAGLE) when the halo mass is smaller than $\approx 3 \times 10^{12} M_\odot$ (Schaye et al. 2015; Schaller et al. 2015). EAGLE has prescriptions for the star formation, stellar evolution, stellar feedback and AGN feedback. The discrepancy between the EAGLE simulations and our models in the high mass region is due to the lack of heating from the AGN feedback in our model, which is positively related to the halo mass rather than the stellar mass. In the low-mass region, the baryonic fraction in our model is slightly less than Schaller et al. (2015) by a factor of $\lesssim 2$ at the halo mass of $10^{11} M_\odot$. This might emphasize the importance of the stellar feedback for the low-mass galaxies, and a γ factor of 0.1–0.2 can account for such a difference. Involving the γ factor described in Section 4.3, we set the upper limits for the baryonic fraction in our models, which is also shown in Fig. 16. The modification on the γ factor leads to higher baryonic fraction in low-mass galaxies, which is consistent with our hypothesis that low-mass galaxies have higher

stellar feedback heating.

However, the trend of increasing baryonic fraction with the halo mass is significantly different from the Illustris simulation, which also has full stellar physics and AGN feedback (Vogelsberger et al. 2014). The Illustris simulation shows the opposite tendency with the low-mass galaxy having more baryonic material (even higher than the cosmic baryonic fraction) enclosed in the virial radius (Suresh et al. 2017). This result may be a result of the photoionization, which is included in Illustris but not EAGLE. Our models show that the photoionization modification is important for low-mass galaxies, since it can support a more massive gaseous halo. Nevertheless, the divergence between Illustris and EAGLE is very unlikely to be caused by the photoionization modification, since it has also been shown that the photoionization can only raise the gaseous halo mass by a factor of about 2, down to the stellar mass of $8 \times 10^7 M_\odot$ (see Section 3.1). This difference is more likely to be caused by the weak stellar feedback employed in Illustris, which is set to keep gas inside the halo (Suresh et al. 2017).

Another consideration that might moderate the missing baryon problem is having a gaseous halo extending beyond the virial radius. When we change the outermost radius for the gaseous halo from one virial radius to twice the virial radius, the gaseous halo mass is increased by a factor of the 2–3. For an L^* galaxy ($M_h = 1.7 \times 10^{12} M_\odot$, $\text{SFR} = 5 M_\odot \text{ yr}^{-1}$), the cooling radius is 173 kpc (less than the virial radius of 253 kpc), which indicates that the increasing of outermost radius will not change the normalization factor in the β -model. Modifying the outermost radius raises the mass from $2.6 \times 10^{10} M_\odot$ to $7.4 \times 10^{10} M_\odot$, raising the baryon fraction from 0.055 to 0.083. Therefore, in the case that the cooling radius is smaller than the virial radius, the factor is fixed to 2.83, otherwise, the factor is slightly smaller but still around 2. This would raise the baryonic fraction, but still not enough to account for all of the missing baryons for L^* galaxies. For the high mass and the low-mass end of the

galaxy distribution, the total baryonic fraction is raised by a factor of ≈ 2 , since most of the mass is in the gaseous halo rather than the stellar content.

4.8. Future Observations

An issue highlighted by this work is that one needs measurements for ions that are the dominant volume filling ions, which traces the gas that is near hydrostatic equilibrium and is at the temperature of most of the gaseous mass. In practice, this requires that we obtain O VII and O VIII absorption line data for galaxies with $M_h > 3 \times 10^{11} M_\odot$. Absorption in O VII is available for the MW for about two dozen sight lines and in O VIII for a handful of objects (Fang et al. 2015; Hodges-Kluck et al. 2016). A significant advance can be realized through improved S/N for O VII and especially O VIII as well as for a larger number of sightlines. This will not happen with existing instruments (*XMM-Newton* and *Chandra*), which have already devoted about 20 Msec of observing time toward bright objects, so improvements would require several times this amount.

For external galaxies, no O VII or O VIII absorption lines have been detected (Nicastro et al. 2016b). Sight lines through the halos of external galaxies ($0.3 - 1 R_{\text{vir}}$) are expected to be nearly an order of magnitude weaker than those from the MW. The failure to see these lines is consistent with model predictions, given the sensitivity of current instruments and the amount of redshift space that has been probed.

Detecting O VII and O VIII through a sample of external galaxy halos will require a new instrument with capabilities that offer at least an order of magnitude improvement. Such an instrument would also offer a breakthrough in the study of these lines in the MW. This level of improvement is possible through *Arcus* (Smith et al. 2016), an Explorer class mission that will have nearly an order of magnitude improvement in both spectral resolution and in collecting area, relative to the *XMM-Newton*/RGS (and a larger improvement relative to the *Chandra*/LETG). The spectral resolution will be about 3000 (100 km s^{-1}), providing kinematic information as well as insights into turbulence. The *Athena* mission will also add to our understanding of these absorption systems, but its spectral resolution is poorer than that of *XMM-Newton* (1300 km s^{-1}), so kinematic information will be limited (Barcons et al. 2017). The *Lynx* mission concept will offer another order of magnitude increase in collecting area, relative to *Arcus* and with double the resolution (50 km s^{-1}), which approaches the thermal width of gas at $2 \times 10^6 \text{ K}$ (Gaskin et al. 2016). It will be sensitive to much weaker lines and will provide excellent kinematic information.

5. SUMMARY

We report upon a gaseous halo model connecting the SFR and the radiative cooling rate, including photoionization and a multi-phase medium. This model predicts a comparable gaseous halo mass to the stellar mass, and can be employed to understand observations of high ionization state ions (i.e., O VI, O VII, Ne VIII, Mg X, and O VIII). We summarize our major results:

1. Photoionization is the most important physical process in determining the relative ion distribu-

tion in the entire extended gaseous halo of low-mass galaxies and the outskirts of massive galaxies. For low-mass galaxies ($M_h < 3 \times 10^{11} M_\odot$), photoionization supports a more massive gaseous halo, and generates high ionization state ions (e.g., O VI and O VII). For more massive galaxies, photoionization leads to more high ionization state ions in the outskirts (i.e., the O VIII of the MW).

2. The multi-phase medium within the cooling radius can be modeled by the distribution of $M(T) \propto T/\Lambda(T)$. This multi-phase medium leads to a flattened dependence of high ionization state ion column densities with galaxy halo mass. More relatively low ionization state ions (compared to the virial temperature) are generated because of the cooling from the high temperature medium.
3. Overall, our models predict the mass of the gaseous halo is comparable to the stellar mass (within one order of magnitude) for star forming galaxies over all halo masses. The cooling radius is expected to vary between 50 – 200 kpc, which is a small variation when compared to the two order of magnitude range in the halo mass.
4. O VI has a narrow range ($\log N(\text{OVI}) = 13.5 - 14.3$) for galaxies with $M_h < 10^{13} M_\odot$. Above $M_h = 3 \times 10^{11} M_\odot$, the O VI is mainly from the collisional ionization, while below this mass, photons from the UVB ionizes most of O VI ions. The predicted O VI column density range is consistent with blind O VI surveys.
5. A modified model is constructed for the Galactic O VII and O VIII, with changes in the standard metallicity of $0.55 Z_\odot$ and a maximum temperature of $1.93 \times 10^6 \text{ K}$, which is above the virial temperature but similar to that derived from emission ratios. Such a gaseous halo leads to a hot halo mass of $1.9 \times 10^{10} M_\odot$ within the virial radius, which contributes to 7% of the total baryonic mass of the MW.
6. For intervening Ne VIII and Mg X at $z = 0.5 - 1.3$, our models predict column densities of $\approx 10^{14} \text{ cm}^{-2}$, which is consistent with observations and informs the detection limit for future observations.
7. Such a gaseous halo cannot close the census of the galaxy missing baryons within R_{vir} . Where it is possible to compare, our models results are similar to those of the EAGLE simulations, and about the half of baryons are still missing for L^* galaxies within the virial radius.

The authors would like to thank the referee for detailed and helpful comments, and Ben Oppenheimer, Edmund Hodges-Kluck, Oleg Gnedin and Hui Li for thoughtful comments and assistance. We also acknowledge the software *Astropy* and *Chianti*, and their developers (Astropy Collaboration et al. 2013; Del Zanna et al. 2015). We gratefully acknowledge support from NASA ADAP

grant NNX16AF23G and from the Department of As-

tronomy at the University of Michigan.

REFERENCES

- Anderson, M. E., & Bregman, J. N. 2010, *ApJ*, 714, 320
- Anderson, M. E., Bregman, J. N., & Dai, X. 2013, *ApJ*, 762, 106
- Anderson, M. E., Churazov, E., & Bregman, J. N. 2016, *MNRAS*, 455, 227
- Armillotta, L., Fraternali, F., & Marinacci, F. 2016, *MNRAS*, 462, 4157
- Armillotta, L., Fraternali, F., Werk, J. K., Prochaska, J. X., & Marinacci, F. 2017, *MNRAS*, 470, 114
- Asplund, M., Grevesse, N., Sauval, A. J., & Scott, P. 2009, *ARA&A*, 47, 481
- Astropy Collaboration, Robitaille, T. P., Tollerud, E. J., et al. 2013, *A&A*, 558, A33
- Baldi, A., Etti, S., Molendi, S., & Gastaldello, F. 2012, *A&A*, 545, A41
- Balogh, M. L., Schade, D., Morris, S. L., et al. 1998, *ApJ*, 504, L75
- Barcons, X., Barret, D., Decourchelle, A., et al. 2017, *Astronomische Nachrichten*, 338, 153
- Behroozi, P. S., Wechsler, R. H., & Conroy, C. 2013, *ApJ*, 770, 57
- Bogdán, Á., Bourdin, H., Forman, W. R., et al. 2017, *ApJ*, 850, 98
- Bogdán, Á., Forman, W. R., Kraft, R. P., & Jones, C. 2013, *ApJ*, 772, 98
- Bregman, J. N. 1980, *ApJ*, 236, 577
- Bregman, J. N., Anderson, M. E., Miller, M. J., et al. 2018, submitted
- Bregman, J. N., & Lloyd-Davies, E. J. 2007, *ApJ*, 669, 990
- Brown, B. A., & Bregman, J. N. 1998, *ApJ*, 495, L75
- Bryans, P., Badnell, N. R., Gorczyca, T. W., et al. 2006, *ApJS*, 167, 343
- Cen, R., & Ostriker, J. P. 1999, *ApJ*, 514, 1
- Chen, H.-W., & Mulchaey, J. S. 2009, *ApJ*, 701, 1219
- Dai, X., Bregman, J. N., Kochanek, C. S., & Rasia, E. 2010, *ApJ*, 719, 119
- Danforth, C. W., & Shull, J. M. 2008, *ApJ*, 679, 194
- Davis, D. S., & White, III, R. E. 1996, *ApJ*, 470, L35
- Del Zanna, G., Dere, K. P., Young, P. R., Landi, E., & Mason, H. E. 2015, *A&A*, 582, A56
- Fabian, A. C. 2012, *ARA&A*, 50, 455
- Faerman, Y., Sternberg, A., & McKee, C. F. 2017, *ApJ*, 835, 52
- Fang, T., Buote, D., Bullock, J., & Ma, R. 2015, *ApJS*, 217, 21
- Fielding, D., Quataert, E., Martizzi, D., & Faucher-Giguère, C.-A. 2017, *MNRAS*, 470, L39
- Fukugita, M., & Peebles, P. J. E. 2006, *ApJ*, 639, 590
- Gaskin, J., Özel, F., & Vikhlinin, A. 2016, in *Proc. SPIE*, Vol. 9904, *Space Telescopes and Instrumentation 2016: Optical, Infrared, and Millimeter Wave*, 99040N
- Gnat, O. 2017, *ApJS*, 228, 11
- Goulding, A. D., Greene, J. E., Ma, C.-P., et al. 2016, *ApJ*, 826, 167
- Grimes, J. P., Heckman, T., Aloisi, A., et al. 2009, *ApJS*, 181, 272
- Gupta, A., Mathur, S., Krongold, Y., Nicastro, F., & Galeazzi, M. 2012, *ApJ*, 756, L8
- Haardt, F., & Madau, P. 2012, *ApJ*, 746, 125
- Henley, D. B., & Shelton, R. L. 2012, *ApJS*, 202, 14
- Hodges-Kluck, E. J., Miller, M. J., & Bregman, J. N. 2016, *ApJ*, 822, 21
- Hopkins, P. F., Kereš, D., Oñorbe, J., et al. 2014, *MNRAS*, 445, 581
- Hopkins, P. F., Wetzell, A., Keres, D., et al. 2017, *ArXiv e-prints*, arXiv:1702.06148
- Hussain, T., Khaire, V., Srianand, R., Muzahid, S., & Pathak, A. 2017, *MNRAS*, 466, 3133
- Hussain, T., Muzahid, S., Narayanan, A., et al. 2015, *MNRAS*, 446, 2444
- Johnson, S. D., Chen, H.-W., & Mulchaey, J. S. 2015, *MNRAS*, 449, 3263
- Johnson, S. D., Chen, H.-W., Mulchaey, J. S., Schaye, J., & Straka, L. A. 2017, *ArXiv e-prints*, arXiv:1710.06441
- Kereš, D., Katz, N., Davé, R., Fardal, M., & Weinberg, D. H. 2009, *MNRAS*, 396, 2332
- Kereš, D., Katz, N., Weinberg, D. H., & Davé, R. 2005, *MNRAS*, 363, 2
- Khaire, V., & Srianand, R. 2015, *MNRAS*, 451, L30
- Kravtsov, A., Vikhlinin, A., & Meshcheryakov, A. 2014, *ArXiv e-prints*, arXiv:1401.7329
- Kwak, K., & Shelton, R. L. 2010, *ApJ*, 719, 523
- Larson, R. B. 1981, *MNRAS*, 194, 809
- Larson, R. B. 1994, in *Lecture Notes in Physics*, Berlin Springer Verlag, Vol. 439, *The Structure and Content of Molecular Clouds*, ed. T. L. Wilson & K. J. Johnston, 13
- Leroy, A. K., Walter, F., Brinks, E., et al. 2008, *AJ*, 136, 2782
- Li, J.-T., Bregman, J. N., Wang, Q. D., Crain, R. A., & Anderson, M. E. 2016, *ApJ*, 830, 134
- . 2017, Submitted
- Li, J.-T., Crain, R. A., & Wang, Q. D. 2014, *MNRAS*, 440, 859
- Li, Y., & Bregman, J. 2017, *ApJ*, 849, 105
- Li, Y., & Bregman, J. 2018, in *American Astronomical Society Meeting Abstracts*, Vol. 231, *American Astronomical Society Meeting Abstracts*, #451.02
- Li, Y., Bryan, G. L., Ruszkowski, M., et al. 2015, *ApJ*, 811, 73
- Lilly, S. J., Carollo, C. M., Pipino, A., Renzini, A., & Peng, Y. 2013, *ApJ*, 772, 119
- Madau, P., & Dickinson, M. 2014, *ARA&A*, 52, 415
- Marinacci, F., Binney, J., Fraternali, F., et al. 2010, *MNRAS*, 404, 1464
- Marinacci, F., Pakmor, R., Springel, V., & Simpson, C. M. 2014, *MNRAS*, 442, 3745
- McGaugh, S. S., & Schombert, J. M. 2015, *ApJ*, 802, 18
- McQuinn, M., & Werk, J. K. 2018, *ApJ*, 852, 33
- Meiring, J. D., Tripp, T. M., Werk, J. K., et al. 2013, *ApJ*, 767, 49
- Ménard, B., Scranton, R., Fukugita, M., & Richards, G. 2010, *MNRAS*, 405, 1025
- Miller, M. J., & Bregman, J. N. 2015, *ApJ*, 800, 14
- Mitra, S., Ferrara, A., & Choudhury, T. R. 2013, *MNRAS*, 428, L1
- Mo, H., van den Bosch, F. C., & White, S. 2010, *Galaxy Formation and Evolution*
- Morselli, L., Renzini, A., Popesso, P., & Erfanianfar, G. 2016, *MNRAS*, 462, 2355
- Muratov, A. L., Kereš, D., Faucher-Giguère, C.-A., et al. 2015, *MNRAS*, 454, 2691
- Myers, P. C., Dame, T. M., Thaddeus, P., et al. 1986, *ApJ*, 301, 398
- Nakanishi, H., & Sofue, Y. 2016, *PASJ*, 68, 5
- Narayanan, A., Savage, B. D., & Wakker, B. P. 2012, *ApJ*, 752, 65
- Nelson, D., Vogelsberger, M., Genel, S., et al. 2013, *MNRAS*, 429, 3353
- Nelson, D., Kauffmann, G., Pillepich, A., et al. 2017, *ArXiv e-prints*, arXiv:1712.00016
- Nevalainen, J., Wakker, B., Kaastra, J., et al. 2017, *A&A*, 605, A47
- Nicastro, F., Senatore, F., Gupta, A., et al. 2016a, *MNRAS*, 457, 676
- . 2016b, *MNRAS*, 458, L123
- Nicastro, F., Zezas, A., Drake, J., et al. 2002, *ApJ*, 573, 157
- Oosterloo, T., Fraternali, F., & Sancisi, R. 2007, *AJ*, 134, 1019
- Oppenheimer, B. D., & Schaye, J. 2013, *MNRAS*, 434, 1043
- Oppenheimer, B. D., Segers, M., Schaye, J., Richings, A. J., & Crain, R. A. 2017, *ArXiv e-prints*, arXiv:1705.07897
- Oppenheimer, B. D., Crain, R. A., Schaye, J., et al. 2016, *MNRAS*, 460, 2157
- Pachat, S., Narayanan, A., Khaire, V., et al. 2017, *MNRAS*, 471, 792
- Pannella, M., Carilli, C. L., Daddi, E., et al. 2009, *ApJ*, 698, L116
- Planck Collaboration, Ade, P. A. R., Aghanim, N., et al. 2016, *A&A*, 594, A13
- Qu, Z., & Bregman, J. N. 2016, *ApJ*, 832, 189
- Renzini, A., & Peng, Y.-j. 2015, *ApJ*, 801, L29
- Robitaille, T. P., & Whitney, B. A. 2010, *ApJ*, 710, L11
- Sancisi, R., Fraternali, F., Oosterloo, T., & van der Hulst, T. 2008, *A&A Rev.*, 15, 189
- Savage, B. D., Kim, T.-S., Wakker, B. P., et al. 2014, *ApJS*, 212, 8
- Savage, B. D., Lehner, N., Wakker, B. P., Sembach, K. R., & Tripp, T. M. 2005, *ApJ*, 626, 776

- Savage, B. D., Sembach, K. R., Wakker, B. P., et al. 2003, *ApJS*, 146, 125
- Scannapieco, C., Tissera, P. B., White, S. D. M., & Springel, V. 2008, *MNRAS*, 389, 1137
- Scannapieco, E., & Brüggen, M. 2015, *ApJ*, 805, 158
- Schaller, M., Frenk, C. S., Bower, R. G., et al. 2015, *MNRAS*, 451, 1247
- Schaye, J., Crain, R. A., Bower, R. G., et al. 2015, *MNRAS*, 446, 521
- Sembach, K. R., Wakker, B. P., Savage, B. D., et al. 2003, *ApJS*, 146, 165
- Smith, R. K., Abraham, M. H., Allured, R., et al. 2016, in *Proc. SPIE*, Vol. 9905, *Space Telescopes and Instrumentation 2016: Ultraviolet to Gamma Ray*, 99054M
- Stern, J., Hennawi, J. F., Prochaska, J. X., & Werk, J. K. 2016, *ApJ*, 830, 87
- Stoche, J. T., Keeney, B. A., Danforth, C. W., et al. 2013, *ApJ*, 763, 148
- . 2014, *ApJ*, 791, 128
- Suresh, J., Rubin, K. H. R., Kannan, R., et al. 2017, *MNRAS*, 465, 2966
- Thom, C., & Chen, H.-W. 2008, *ApJS*, 179, 37
- Thompson, T. A., Quataert, E., Zhang, D., & Weinberg, D. H. 2016, *MNRAS*, 455, 1830
- Tripp, T. M., Meiring, J. D., Prochaska, J. X., et al. 2011, *Science*, 334, 952
- Tumlinson, J., Peebles, M. S., & Werk, J. K. 2017, *ARA&A*, 55, 389
- Tumlinson, J., Thom, C., Werk, J. K., et al. 2011, *Science*, 334, 948
- Vogelsberger, M., Genel, S., Springel, V., et al. 2014, *MNRAS*, 444, 1518
- Wang, Q. D., Yao, Y., Tripp, T. M., et al. 2005, *ApJ*, 635, 386
- Weinberg, D. H., Miralda-Escudé, J., Hernquist, L., & Katz, N. 1997, *ApJ*, 490, 564
- Werk, J. K., Prochaska, J. X., Thom, C., et al. 2013, *ApJS*, 204, 17
- Werk, J. K., Prochaska, J. X., Tumlinson, J., et al. 2014, *ApJ*, 792, 8
- White, S. D. M., & Frenk, C. S. 1991, *ApJ*, 379, 52
- Wiersma, R. P. C., Schaye, J., & Smith, B. D. 2009, *MNRAS*, 393, 99
- Willson, L. A. 2000, *ARA&A*, 38, 573
- Zaritsky, D., Kennicutt, Jr., R. C., & Huchra, J. P. 1994, *ApJ*, 420, 87
- Zheng, Y., Peek, J. E. G., Werk, J. K., & Putman, M. E. 2017, *ApJ*, 834, 179